Measuring the ion-specific heat of electrical double layer formation in porous carbon

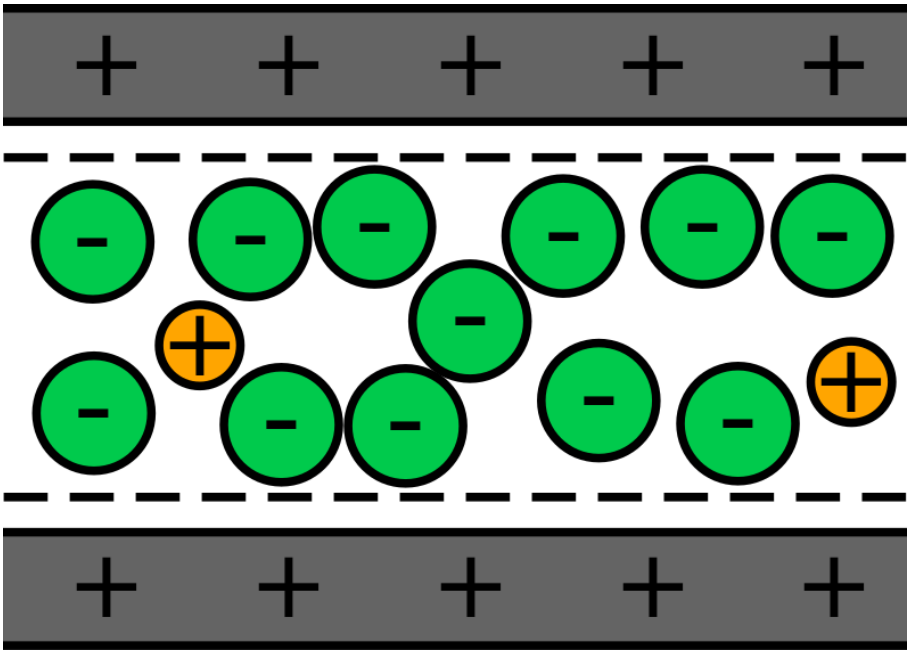

H.P. Rodenburg

Master's thesis for the Nanomaterials Science programme

Under the supervision of J.E. Vos and Dr. B.H. Erné

Van 't Hoff Laboratory for Physical and Colloid Chemistry
Debye Institute for Nanomaterials Science
Utrecht University

30 January 2020

Abstract

The reversible heat of electrical double layer (EDL) formation in porous carbon has been investigated several times since 2006, typically by measuring the combined heat production of the anode and the cathode in an electrochemical cell. In this work, the heat of EDL formation is instead determined at one electrode. Our aim is to use this approach to determine the EDL formation heat for one type of counterion at a time.
To measure the EDL formation heat at one electrode, two calorimetric setups are built, both of which contain a three-electrode cell in which only the heat generated at the working electrode is measured. The first setup uses thermometers to conduct a temperature difference measurement, while the second measures the heat directly using a heat flux sensor.
The reversible heat, which is the heat of EDL formation, can be separated from the irreversible heat by comparing the total measured heat during charging and discharging. Results obtained with the temperature difference measurement setup show that the heat of EDL formation is higher with Cl^- or F^- counterions than with Na^+ counterions. This is ascribed to different ionic radii giving rise to different entropic changes during EDL charging. A simple, exclusively entropic model is developed based on this concept. It is capable of reproducing the experimental results with reasonable ionic radii and micropore volume as input. Accounting for the ionic radii appears to be necessary to explain the difference in EDL formation heat between Na^+ counterions and Cl^- or F^- counterions.

Contents

1 Introduction

Electrical double layers (EDLs) are structures consisting of a charged object or surface and a layer of counterions, as illustrated in Figure 1. Electrical double layers are ubiquitous: they form around colloids, on electrodes and on various other charged surfaces. EDLs have been the subject of scientific investigation for over a century and continue to be studied actively to this day [1].

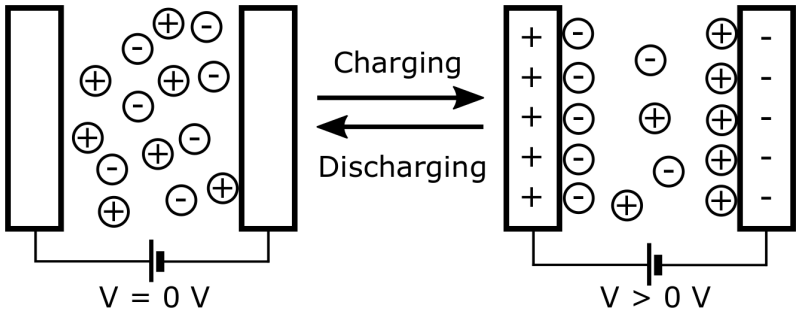

Figure 1: Schematic illustration of EDL formation on two charged surfaces. One EDL is formed on each surface. The surfaces are charged up by applying a potential difference between them.

One important system in which EDLs are formed is the water desalination process called *capacitive deionisation* (CDI). Water desalination processes are employed to turn brackish water into drinkable freshwater, which will likely be available in decreasing quantities from natural sources due the growing world population and changes in the worldwide climate [2, 3].
In CDI, brackish water is led into a compartment in which two porous carbon electrodes draw in anions and cations when a voltage is applied. The salt concentration in the water drops as ions accumulate in the pores of the electrodes. Once the EDLs in the electrodes are fully charged, the desalinated water is removed from the compartment [2]. While the focus of this work is not on CDI, it is on EDLs in porous carbon, and the porous carbon used in this work is the same material that is used in CDI.

The porous carbon material typically used for CDI electrodes is activated carbon, which has a large (1000 – 3500 m^2g^{-1}) specific surface area [2]. As a result, many ions can adsorb in the material's pores. The area of the smallest pores, the micropores ($d < 2$ nm), is particularly important in this regard [2]. The ability of a CDI electrode to store many ions translates to a high (ca. 20 Fg^{-1}) capacitance [4, 5].

Most of our knowledge about EDLs in porous carbon electrodes comes from electrochemical analyses and analyses of salt concentration. These can give information about the capacitance and rate of charging of an EDL in porous carbon and about the occurrence of any electrochemical side-reactions. However, several other properties of the EDL, such as changes in enthalpy and entropy during charging and discharging, cannot be investigated through electrical measurements alone. To investigate these properties, we will measure the heat of EDL formation. This is a tiny heat effect, but the high capacitance of porous carbon allows an EDL to be formed inside that is sufficiently large for its heat of formation to be measurable, which is practically impossible for a flat plate EDL.

There have been few investigations into the heat of EDL formation since the first measurements were reported 15 years ago. In 2005, heating was studied in commercial supercapacitors by *Schiffer et al.* [6]. More than a decade later, heat effects in carbon electrodes in purpose-built electrochemical cells were investigated by *Janssen et al.* [7] and *Munteshari et al.* [8] In both of these studies, a CDI-style system with two parallel porous carbon electrodes in close proximity to each other was used, as schematically illustrated in Figure 2 [7, 8].

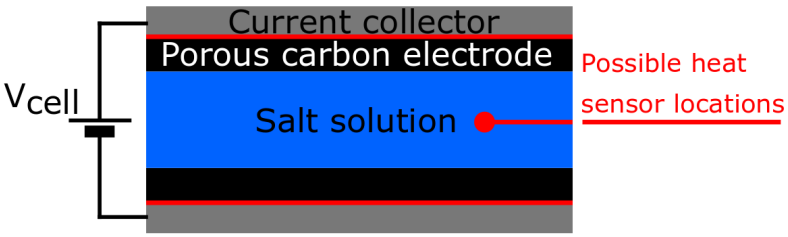

Figure 2: Schematic drawing of a two-electrode cell for heat measurements.

Measuring the heat of EDL formation requires the presence of a heat sensor of some kind, such as a thermometer or a heat flux sensor [6–8]. The latter typically takes the form of thermoelectric PVDF foil or an array of thermocouples connected in series [8, 9]. One procedure for using a heat sensor to obtain the EDL formation heat is a chronoamperometric *voltage step* experiment. In this type of measurement, the current and heat are measured while the electrodes are charged by applying a cell voltage $V_{cell} > 0$ V for several hours and discharged by applying $V_{cell} = 0$ V for the same duration. The reversible heat generated during such a charge-discharge cycle is twice the heat of EDL formation [7].

While the work done by *Janssen et al.* [7] and *Munteshari et al.* [8] has been useful by providing insight into the heat of EDL formation, by sparking theoretical studies and by demonstrating highly effective calorimetric measurement methods, the results are still limited due to the use of a two-electrode cell with only a small amount of electrolyte solution between the electrodes [7, 8, 10, 11]. When one measures the heat of EDL formation in a cell with two electrodes in close proximity to each other, the measured heat of EDL formation is due to both an EDL in the anode and an EDL in the cathode, whose counterions are anions and cations respectively. The contributions of the two ionic species are difficult to separate.

The aim of this work is to measure the heat of EDL formation for one type of counterion. This will require the construction of a cell that is optimised for measurements at one electrode.

2 Theoretical background

2.1 Electrical double layers at flat electrodes

The most well-known theories of electrical double layers are Gouy-Chapman theory, also known as Poisson-Boltzmann theory, and Otto Stern's modification of the theory. Although other, more modern theoretical models have emerged since Gouy-Chapman-Stern theory came about in 1924, the theory still provides an acceptable description of the electrical double layer in certain cases [12–15].

The following introduction of Gouy-Chapman theory is based on Schmickler's *Interfacial Electrochemistry* [15]. Consider a system in which a two-dimensional, planar electrode is located at $x = 0$. The electrode has a surface charge density σ. There is potential ψ, which is related to the charge density in the solution ρ via the Poisson equation, Equation 1. In this equation, ϵ_0 is the vacuum permittivity and ϵ_r is the relative permittivity of the medium.

$$\frac{\mathrm{d}^2\psi}{\mathrm{d}x^2} = \frac{-\rho(x)}{\epsilon_r\epsilon_0} \tag{1}$$

The charge density in the solution is dependent on the concentrations of the ions, following Equation 2.

$$\rho(x) = ze[n_+(x) - n_-(x)] \tag{2}$$

Choosing $\psi(\infty) = 0$ and applying Boltzmann statistics gives Equations 3 and 4:

$$n_+(x) = n_0 \exp\left[- \frac{ze\psi(x)}{kT}\right] \tag{3}$$

$$n_-(x) = n_0 \exp\left[+ \frac{ze\psi(x)}{kT}\right] \tag{4}$$

where $n_0 = n_+(\infty) = n_-(\infty)$, the bulk ion concentration.

Substituting Equations 3 and 4 into Equation 2 and then substituting Equation 2 into Equation 1 results in Equation 5, the Poisson-Boltzmann Equation.

$$\frac{\mathrm{d}^2\psi}{\mathrm{d}x^2} = \frac{-zen_0}{\epsilon_r\epsilon_0}\left[\exp\left(- \frac{ze\psi(x)}{kT}\right) - \exp\left(+ \frac{ze\psi(x)}{kT}\right)\right] \tag{5}$$

The Poisson-Boltzmann equation may be linearised if $ze\psi(x)/(kT) << 1$, resulting in Equation 6. The screening constant κ in equation 6 is the inverse of the Debye screening length for a symmetric, two-component electrolyte. The Debye screening length quantifies up to what distance the electrostatic effects of charged objects are felt.

$$\frac{\mathrm{d}^2\psi}{\mathrm{d}x^2} = \kappa^2\psi(x); \kappa = \sqrt{\frac{2N_{Av}(ze)^2n_0}{\epsilon_r\epsilon_0 kT}} \tag{6}$$

Equation 6 may be solved if $\psi(\infty) = 0$. The solution takes the form of Equation 7.

$$\psi(x) = A\exp[-\kappa x] \tag{7}$$

In Equation 7, the pre-factor A is fixed by the charge balance condition, Equation 8, in which σ is the surface charge density.

$$\int_0^\infty \rho(x)\,\mathrm{d}x = -\sigma \tag{8}$$

From Equations 7 and 8, an expression for the potential ψ can be obtained.

$$\psi(x) = \frac{\sigma}{\epsilon_r \epsilon_0 \kappa} \exp[-\kappa x] \tag{9}$$

From here, an expression for the charge density in solution ρ can be obtained. First, Equation 6 is combined with Equation 1 to give Equation 10.

$$\kappa^2 \psi(x) = \frac{-\rho(x)}{\epsilon_r \epsilon_0} \tag{10}$$

Then, inserting Equation 9 into Equation 10 yields Equation 11 for $\rho(x)$.

$$\rho(x) = -\sigma \kappa \exp[-\kappa x] \tag{11}$$

Finally, the linearised Poisson-Boltzmann equation also yields an expression for the capacitance of the electrical double layer. This is Equation 12.

$$C = \epsilon_r \epsilon_0 \kappa \tag{12}$$

This solution only holds for low surface charge densities, due to the linearisation. Without linearisation, the capacitance is given by Equation 13. For a 1:1-electrolyte, the capacitance then follows the plot in Figure 3. The full derivation of Equation 13, starting from Equation 5, can be found in *Interfacial Electrochemistry* [15].

$$C = \epsilon_r \epsilon_0 \kappa \cosh\left[\frac{ze\psi)}{2kT}\right] \tag{13}$$

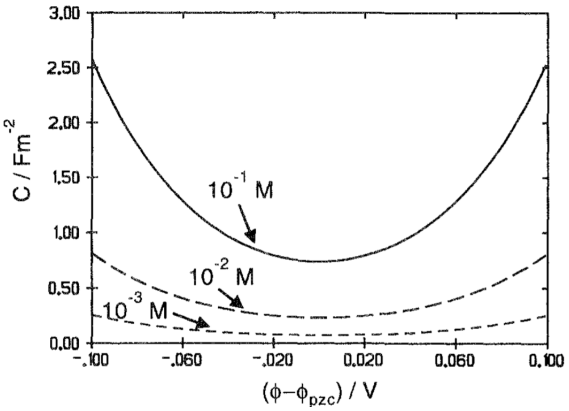

Figure 3: Gouy-Chapman capacitance for a 1:1-electrolyte at different concentrations and different potentials $\phi - \phi_{pzc}$, where ϕ_{pzc} is the equilibrium potential. Taken from *Interfacial Electrochemistry* [15]. Note that ϕ_{pzc} is called ψ_{zc} in the rest of this work.

While non-linear Gouy-Chapman theory can account for higher surface charge densities σ than the linear version of the theory, it still fails once the surface charge density becomes too high. Additionally, non-linear Gouy-Chapman theory also breaks down when the ions' concentrations become too high. When the theory breaks down, the capacitance no longer follows Equation 13. The capacitance instead follows Equation 14, in which C_{GC} is the Gouy-Chapman capacitance and C_H is the Helmholtz capacitance [15].

$$\frac{1}{C} = \frac{1}{C_{GC}} + \frac{1}{C_H} \tag{14}$$

The cause of deviations from the Gouy-Chapman capacitance is the presence of a non-diffuse part of the electrical double layer. This part of the double layer forms due to the finite size of

the counterions and water molecules. Otto Stern's modification of the theory accounts for the finite size of the ions and water molecules by assuming that an adsorbed layer of counterions, which are surrounded by water molecules, covers the charged surface [14]. Beyond this layer, at a distance equal to at least the diameter of the hydrated ions, Gouy-Chapman theory takes over. This is known as Gouy-Chapman-Stern theory.

While Gouy-Chapman-Stern theory provides an explanation for some systems that exhibit non-Gouy-Chapman behaviour, it too breaks down at high concentrations of ions and at high surface charge densities. Several other theories have been developed to describe systems with these features [16] and significant progress has been made in simulations of electrical double layers since the 1980s [17–20]. Recently, Density Functional Theory has also been employed to study EDLs [21, 22]. However, despite these developments, the Gouy-Chapman-Stern view of the EDL remains common in literature.

2.2 Formation of EDLs

The formation of an electrical double layer involves a change in the free energy of the system. Both enthalpic and entropic effects play a role in EDL formation [23, 24]. The enthalpic effect is related to the electrostatic interactions between the ions and charged surfaces, as well as between different ions. The entropic effect, on the other hand, is related to the ions ordering into an EDL, which affects the freedom of movement of the ions. These effects have been investigated theoretically by *Overbeek* [23].

The system under consideration is very general: charged colloidal particles of arbitrary shape are present in an aqueous electrolyte solution. The particles' surfaces have a surface charge density σ and a surface potential ϕ_0. The surfaces are described by surface elements $\mathrm{d}A$. Similarly, the electrolyte solution has a volume charge density ρ and a a potential ϕ. Its volume is described in terms of volume elements $\mathrm{d}V$. There are dimensionless potentials $\phi = \frac{e\psi}{kT}$ and $\phi_0 = \frac{e\psi_0}{kT}$. The screening constant κ takes the general form shown in Equation 15 [23].

$$\kappa = \sqrt{\frac{\sum_i n_{i0}(z_i e)^2}{\epsilon_r \epsilon_0 kT}} \tag{15}$$

The system is incompressible. Therefore, the Helmholtz free energy F_{el} equals the Gibbs free energy G_{el}. The free energy F_{el} consists of an electrostatic energy term U_{el} and an entropic term $-T\Delta S$, as in Equation 16 [23].

$$F_{el} = U_{el} - T\Delta S \tag{16}$$

The energy term is given by Equation 17 and the entropy term is given by Equation 18. For the full derivation, see the work by *Overbeek* [23].

$$U_{el} = \frac{\epsilon_r \epsilon_0}{2} \int_V (\nabla\psi)^2 \,\mathrm{d}V \tag{17}$$

$$-T\Delta S = \epsilon_r \epsilon_0 \int_V \psi \nabla^2 \psi \,\mathrm{d}V - \epsilon_r \epsilon_0 \int_V \mathrm{d}V \int_0^\psi \nabla^2 \psi \,\mathrm{d}\psi \tag{18}$$

The free energy follows directly from Equations 17 and 18:

$$F_{el} = \epsilon_r \epsilon_0 \int_V \left[\frac{(\nabla\psi)^2}{2} + \psi\nabla^2\psi - \int_0^\psi \nabla^2\psi \,\mathrm{d}\psi \right] \mathrm{d}V = \epsilon_r \epsilon_0 \int_V \left[\int_0^\psi \nabla\psi \,\mathrm{d}(\nabla\psi) + \int_0^\psi \psi \,\mathrm{d}(\nabla^2\psi) \right] \mathrm{d}V \tag{19}$$

Using Green's formula [25], this result is found to correspond to the result obtained via an imaginary charging process, Equation 20 [23].

$$F_{el} = \int_A \int_{\sigma=0}^{\sigma_{final}} \psi_0 \, \mathrm{d}\sigma \, \mathrm{d}A \tag{20}$$

From Equation 19, it is apparent that U_{el} and $-T\Delta S$ are both positive. In the absence of any chemical driving force, they work together in the formation of an electrical double layer when the surface charge density σ is increased. This can be clearly seen in Equation 20, which shows that increasing σ has only one, positive, effect on F_{el} [23].

While the field energy and entropy always work together according to this model, they do not always contribute equally. At low surface potentials, the field energy and entropy terms are roughly equal, whereas at high surface potentials, the entropy term dominates. It should be noted that this is only the case in this simple model, which does not account for the structure adopted by water in the system. In reality, the existence of this structure means U_{el} is a free energy: an additional entropic contribution is involved within this term [23].

2.3 Effects of ionic radius

The effects of the ionic radius of the counterions on the properties of the electrical double layer have been treated by *Biesheuvel and Soestbergen* [26], using Poisson-Boltzmann theory modified to include non-electrostatic interactions. Specifically, interactions between hard spheres of unequal sizes are considered [26].

The ions' concentrations are determined using Poisson-Boltzmann theory, specifically using Equation 21, the equality of chemical potentials. In this equation, μ_i^{ex} and $\mu_{i,\infty}^{ex}$ are the chemical potentials of the ions i in the EDL and in bulk, respectively. Similarly, n_i and $n_{i,\infty}$ are their concentrations in the EDL and in bulk. The ions' valency is given by the integer z_i and the dimensionless potential is denoted ψ [26].

$$\ln n_{i,\infty} + \mu_{i,\infty}^{ex} = \ln n_i + z_i\psi + \mu_i^{ex} \tag{21}$$

Ions are treated not just as point charges, but also as hard spheres of unequal sizes. For hard spheres of unequal sizes, the Boublik-Mansoori-Carnahan-Starling-Leland equation of state is used. See Equation 22. In this equation, which gives the chemical potential for ionic species i, σ_i is the ionic radius, $\xi_k = \sum_j \phi_j \sigma_j^{k-3}$ and ϕ is the occupied volume of all ions combined, which follows from the ionic radii σ_j and concentrations n_j of all ions j as $\phi = \sum_j n_j v_j$. In the expression for ξ_k, j runs over all particles and $k = 0, 1$ or 2 [26, 27].

$$\begin{aligned} \mu_i^{ex} = -\left(1 + \frac{2\xi_2^3\sigma_i^3}{\phi^3} - \frac{3\xi_2^2\sigma_i^2}{\phi^2}\right)\ln(1-\phi) + \frac{3\xi_2\sigma_i + 3\xi_1\sigma_i^2 + \xi_0\sigma_i^3}{1-\phi} \\ + \frac{3\xi_2\sigma_i^2}{(1-\phi)^2}\left(\frac{\xi_2}{\phi} + \xi_1\sigma_i\right) - \xi_2^3\sigma_i^3\frac{\phi^2 - 5\phi + 2}{\phi^2(1-\phi)^3} \end{aligned} \tag{22}$$

Equation 22 can be used to add a third term to the Helmholtz free energy of the electrical double layer. Besides the field energy and entropy terms treated in section 2.2, a volume exclusion term is now added. This term is added to the free energy via the position-dependent free energy density $\omega(x)$, from which the free energy F follows via $F = \int_{x=0}^{\infty} \omega(x) \, \mathrm{d}x$ [26].

The system described by *Biesheuvel and Soestbergen* [26] is not as general as the one described by *Overbeek* [23]. The system under consideration here is a simple model system, in which an EDL forms at a two-dimensional, planar electrode with a fixed surface charge density Σ. In this system, the entropy, field energy and volume exclusion terms are given by Equations 23–25 [26].

$$\omega^{S_{ion}} = \sum_j \left[n_j \ln n_j - \ln n_{j,\infty} - (n_j - n_{j,\infty})\right] \tag{23}$$

$$\omega^{U_{field}} = \frac{1}{8\pi\lambda_B}\left(\frac{d\psi}{dx}\right)^2; \lambda_B = \frac{e^2}{4\pi\epsilon_r\epsilon_0 kT} \tag{24}$$

$$\omega^{ex} = \frac{6}{\pi}\left(-\xi_0 \ln(1-\phi) + 3\frac{\xi_1\xi_2}{1-\phi} + \xi_2^3 \frac{\phi + (1-\phi)^2\ln(1-\phi)}{\phi^2(1-\phi)^2}\right) \tag{25}$$

In these equations, x is the distance from the electrode and λ_B is the *Bjerrum length*, which is the distance at which the interaction energy between two ions is equal to kT. If all ionic radii are equal, the various ξ_k disappear and Equation 25 reduces to Equation 26, in which v is the volume of a single ion [26].

$$\omega^{ex} = \frac{1}{v}\int_{x=0}^{\infty} \frac{\phi(4\phi - 3\phi^2)}{(1-\phi)^2}\,\mathrm{d}x \tag{26}$$

The contributions of the three free energy terms are separately evaluated and plotted in Figure 4 for a 1:1-electrolyte with equal (3.3 Å) radii for the anions and cations. At low surface charge densities, the entropy and electric field energy terms are equally important, while entropy dominates at slightly higher surface charge densities. The new term, the volume exclusion term ω^{ex}, becomes more important with increasing surface charge density. At even higher surface charge densities, everything changes. The electric field energy term now overtakes the entropy term, while the volume exclusion term continues to grow and eventually overtakes the entropy term, but not the field energy term [26].

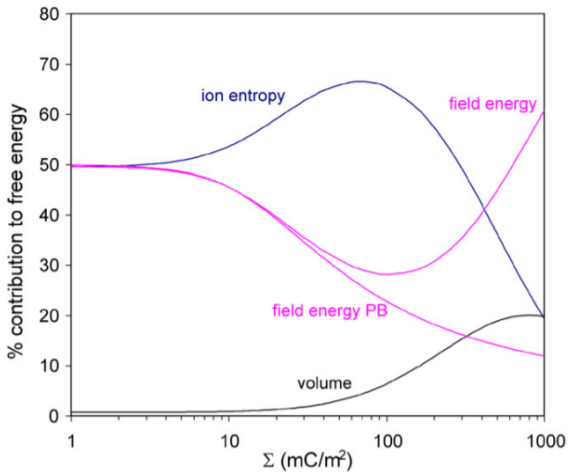

Figure 4: Terms of the free energy in a system with a hard-sphere ion EDL. Σ is the surface charge density. Taken from *Biesheuvel and Soestbergen.* [26]

While this result seems to indicate that the field energy is very important and that volume exclusion only matters at very high surface charge densities, it is important to note that the result is obtained for the simplest EDL geometry. It does not necessarily translate well to EDLs in porous networks.

2.4 EDLs in porous carbon

Electrical double layers in porous carbon are not directly comparable to the flat plate EDLs under consideration in section 2.3. This is due to the Debye screening length typically being much larger than the average pore size. As a result, the double layers in the pores' interiors are strongly overlapping [28]. See Figure 5.

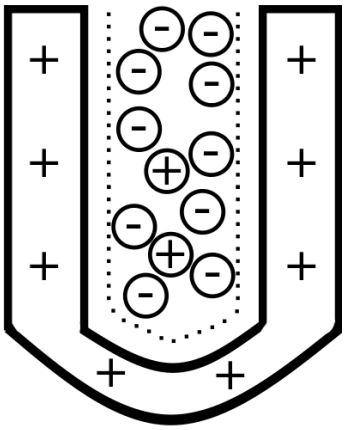

Figure 5: The EDLs in porous carbon's pores are strongly overlapping. The dotted lines indicate the region that is inaccessible to the ions, due to the presence of water molecules. They give an impression of the Stern layer.

The strong overlap of the double layers leads to a constant potential inside the pores. Consequently, there is hardly any electric field inside the pores. As such, the field energy term described in previous sections becomes negligible. The ion entropy and volume exclusion terms, which are both entropic, remain.

The lack of a potential difference inside the pores allows a modified version of the constant-potential Donnan model, developed by *Porada et al.* [28], to be applied. Two modifications are made to the well-known Donnan model. Firstly, a dielectric capacitance between the electrode and the ions is included to account for the Stern layer. Secondly, a chemical attraction energy μ_{att} for the ions transferring into the pores is included. With these modifications, the concentration of ions in the pores is given by Equation 27, in which $\Delta\phi_d$ is the Donnan potential difference between the porous network and the bulk solution outside it [28].

$$c_j^{pores} = c_{salt}^{bulk} \times \exp(-z_j \Delta\phi_d + \mu_{att}) \tag{27}$$

The concentrations of the anions and cations are affected by any charge borne by the porous network. Given a charge density ρ in the porous network, the concentrations of the cations and anions, denoted c_+^{pores} and c_-^{pores} respectively, change following Equation 28 [28].

$$\rho = c_+^{pores} - c_-^{pores} = -\frac{RT}{F^2}\Delta\phi_{St} C_{St}^{vol} \tag{28}$$

The potential difference $\Delta\phi_{St}$ is the potential drop over the Stern layer and C_{St}^{vol} is the Stern layer's volumetric capacity. The Donnan potential difference and the potential drop over the Stern layer can be combined to give the cell voltage V_{cell}, following Equation 29, if the system is in equilibrium [28].

$$V_{cell} = \frac{2RT}{F}\big(\Delta\phi_d + \Delta\phi_{St}\big) \tag{29}$$

Using Equations 27–29 and an empirical expression for the volumetric Stern layer capacity, it is possible to calculate the experimentally measurable *salt adsorption* Γ_{salt} and *equilibrium charge* Σ_F following Equations 30 and 31 respectively [28].

$$\Gamma_{salt} = \frac{1}{2}\nu\big[(c_+^{pores} - c_-^{pores}) - (c_+^{pores} - c_-^{pores})^0\big] \tag{30}$$

$$\Sigma_F = -\frac{1}{2}F\nu\rho \tag{31}$$

In both equations, ν is the micropore volume per unit electrode mass. In Equation 30, the term with superscript 0 is the total ion concentration when no potential is applied. These equations can reproduce experimental data quite well for a variety of porous carbon materials, although this does require the use of the fitting parameters α and ${C_{St}^{vol}}^0$ to determine C_{St}^{vol}. The volumetric Stern layer capacity follows from these parameters via $C_{St}^{vol} = {C_{St}^{vol}}^0 + \alpha\rho^2$. When the parameters are given the appropriate values, results like those in Figure 6 can be obtained, as was done by *Porada et al.* [28]

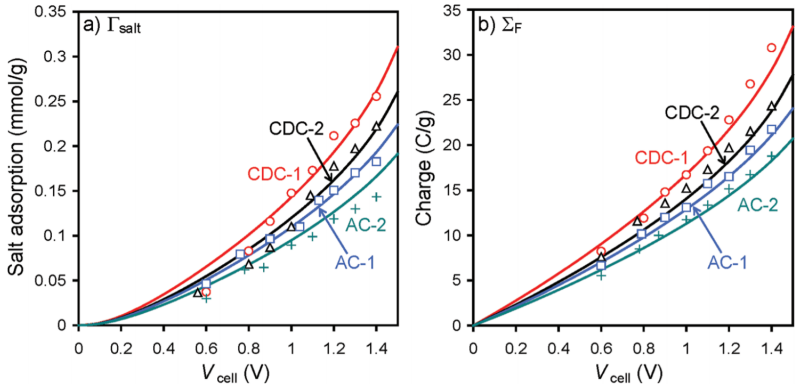

Figure 6: Salt adsorption and equilibrium charge for several types of porous carbon. Markers indicate experimental data. Lines are fitted using the modified Donnan model. ${C_{St}^{vol}}^0 = 190$ MFm^{-3} for AC-2 and 200 MFm^{-3} for CDC-1, CDC-2 and AC-1. For CDC-1 and CDC-2, $\alpha = 21.7$ Fm^{3}mol^{-2}, while $\alpha = 19.2$ Fm^{3}mol^{-2} for AC-1 and AC-2. Figure taken from *Porada et al.* [28]

The experimental data and the model are in good agreement with one another. Perhaps other types of experimental data could also be explained using the modified Donnan model. While the model has not been further developed to predict the changes in enthalpy and entropy during EDL formation, doing so in the near future might be a worthwhile effort.

2.5 Heat of EDL formation

To investigate the enthalpic and entropic contributions to the change in free energy upon formation of an electrical double layer experimentally, one should measure the heat of EDL formation. The change in free energy during charging is equal to the heat of EDL formation, which is measurable as half of the difference in heat production between charging and discharging, assuming the irreversible heat production is the same during charging and discharging. There have been several experimental and theoretical investigations into the heat of EDL formation [6, 7, 10, 11, 29].

The experimentally measured heat Π consists of the desired reversible contribution and an irreversible contribution [6, 7]. These two contributions are defined for a charge-discharge cycle from t_0 to t_2, with the EDL being charged between t_0 and t_1 and it being discharged between t_1 and t_2 [7].

$$\int_{t_0}^{t_2} \dot{\Pi}(t)\,\mathrm{d}t = \Pi = \Pi_{rev} + \Pi_{irr} \tag{32}$$

The irreversible heating term results from Joule heating in the circuit. The Joule heat follows from the time-integrated product of the current and the voltage. In the case of an EDL, the relevant voltage is the voltage over the solution and other resistive parts of the circuit. This voltage ψ_R is lower than the applied voltage ψ, because the applied voltage is diminished inside the electrical double layer, which acts as a capacitor. The voltage drop over the EDL is denoted

ψ_C. Thus, the voltage across the resistive components is $\psi_R = \psi - \psi_C$, which depends on the capacitance C and the build-up of charge $Q(t)$ in the EDL. See Equation 33 [7].

$$\psi_R(t) = \psi - \psi_C(t) = \psi - \frac{Q(t)}{C} = \psi\left[1 - \frac{\int_{t_0}^{t} I(t')\,\mathrm{d}t'}{\int_{t_0}^{\infty} I(t'')\,\mathrm{d}t''}\right] \tag{33}$$

In practice, the infinity in Equation 33 is approximated by taking the time $\tau = t_2 - t_1 = t_1 - t_0$ during a long charging or discharging period. As such, $\int_{t_0}^{\infty} I(t'')\,\mathrm{d}t''$ becomes $\int_{t_0}^{t_1} I(t'')\,\mathrm{d}t''$. Once calculated, the voltage across the solution and other resistive, heat-dissipating elements goes into the expression for irreversible heating, Equation 34 [7].

$$\Pi_{irr} = \int_{t_0}^{t_2} I(t)\psi_R(t)\,\mathrm{d}t \tag{34}$$

The irreversible heat is needed to determine the coefficient of heat transfer K, which serves as a calibration constant for the heat sensor. The total heat generated during charging and discharging is measured with a temperature difference measurement setup. In a charge-discharge cycle, the net reversible heat is zero, and thus the total temperature difference in a cycle originates only from irreversible heating. Therefore, the temperature difference can be calibrated against the irreversible heat to obtain K following Equation 35 [7].

$$\int_{t_0}^{t_2} I(t)\psi_R(t)\,\mathrm{d}t = K\int_{t_0}^{t_2} \Delta T(t)\,\mathrm{d}t \tag{35}$$

Although K is in principle defined for each charge-discharge cycle, there can be only one coefficient of heat transfer for a given setup. Therefore, K is determined from a linear regression through the origin in a $\big(\int_{t_0}^{t_2} I(t)\psi_R(t)\,\mathrm{d}t, \int_{t_0}^{t_2} \Delta T(t)\,\mathrm{d}t\big)$-plot. As soon as K is known, the reversible heat can be determined. The reversible heating term is the formation heat of the electrical double layer. This heat may be determined via Equation 36 [7].

$$\Pi_{rev} = \Pi_{rev}^{charge} = -\Pi_{rev}^{disch} = \frac{\Pi_{tot}^{charge} - \Pi_{tot}^{disch}}{2} = \frac{K\big[\int_{t_0}^{t_1} \Delta T(t)\,\mathrm{d}t - \int_{t_1}^{t_2} \Delta T(t)\,\mathrm{d}t\big]}{2} \tag{36}$$

Similarly, the irreversible heat now follows from Equation 37.

$$\Pi_{irr} = \Pi_{irr}^{charge} = -\Pi_{irr}^{disch} = \frac{\Pi_{tot}^{charge} + \Pi_{tot}^{disch}}{2} = \frac{K\big[\int_{t_0}^{t_1} \Delta T(t)\,\mathrm{d}t + \int_{t_1}^{t_2} \Delta T(t)\,\mathrm{d}t\big]}{2} \tag{37}$$

To see why the reversible heat follows from the difference between the heats of charging and discharging, consider Figure 7. The irreversible heat is (assumed to be) equal during charging and discharging, but the reversible heat's sign changes, although its magnitude remains the same. When the EDL is charged, the measured heat is increased by the heat of EDL formation, but when the EDL is discharged, the measured heat is decreased by the same amount. Thus, the average measured heat during charging and discharging is the irreversible heat, while the difference between the measured heats is *twice* the heat of EDL formation.

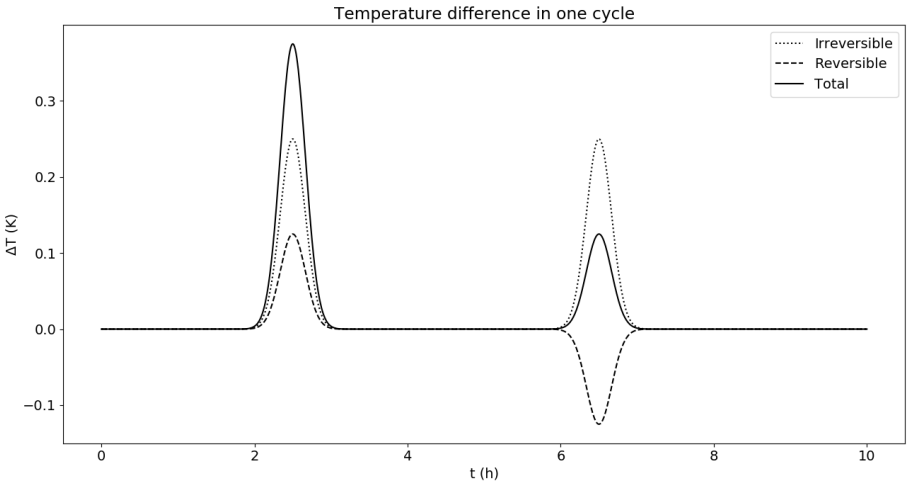

Figure 7: The reversible and irreversible contributions to the temperature difference peaks in one charge-discharge cycle. The peak shapes are not representative of a real measurement result.

In experiments by *Janssen et al.* [7], the heat of EDL formation is determined in a two-electrode cell, in which a non-zero voltage is applied between the working and counter electrodes to charge an EDL at each electrode. To discharge the EDLs, the applied voltage is set to 0 V. Charging and discharging both take four hours. The reversible heat is determined through a temperature difference measurement between two thermometers. The setup and cell are shown in Figure 8 [7].

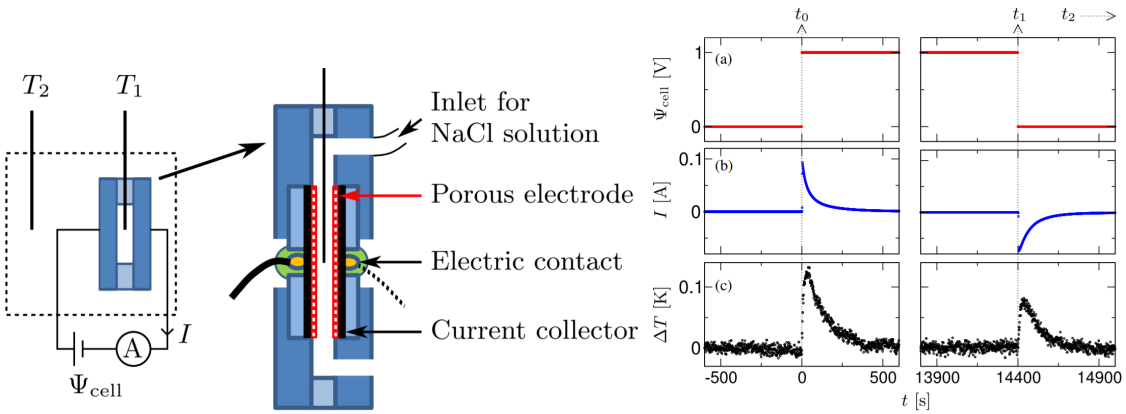

Figure 8: The two-electrode cell used by *Janssen et al.* [7] A measurement result obtained with the setup is shown on the right. The environment in which the cell and T_2 are located is thermostatted. Figures taken from *Janssen et al.* [7]

In this work, the calibration method works very well. See Figure 9.

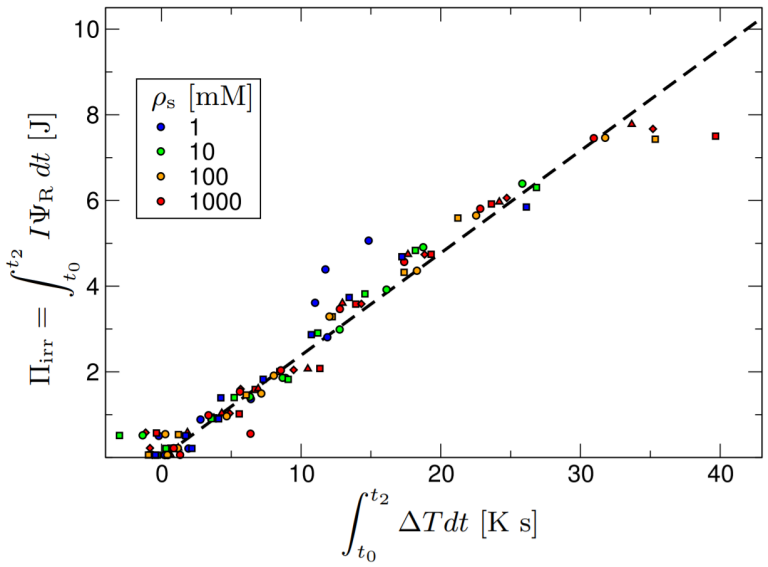

Figure 9: Calibration of the temperature difference measurement setup used by *Janssen et al.* [7], following Equation 35. ρ_s is the salt concentration. Figure taken from *Janssen et al.* [7]

Using the slope of the line in Figure 9 as the coefficient of heat transfer, the heat of EDL formation can be determined. See Figure 10.

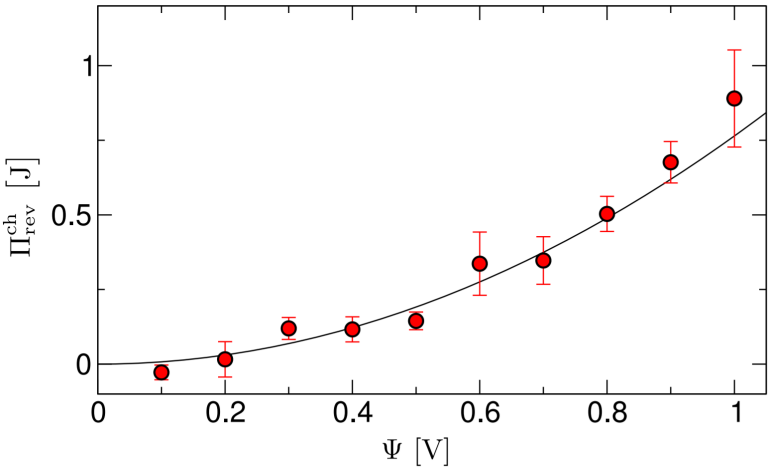

Figure 10: The heat of EDL formation for 1 M NaCl, as determined by *Janssen et al.* [7] in their two-electrode cell. Figure taken from *Janssen et al.* [7]

While the methods of *Janssen et al.* [7] can be used to determine the heat of EDL formation for the whole cell, a shortcoming in the design of the two-electrode cell prevents the separate investigation of different ionic species. In the cell, the working and counter electrodes are placed so close together that the formation heat of two EDLs is measured, instead of the formation heat of one. In the anode, an EDL is formed with anions as counterions and in the cathode, an EDL with cations as counterions is formed. The contributions of the two types of ions to the heat of EDL formation cannot be separated, due to the proximity of the two electrodes. Separating the effects of the cations from those of anions would allow one ionic species to be studied at a time, which would in turn allow the effects of ionic radius and valency on the heat of EDL formation to be studied.

3 Experimental methods

3.1 Measurements at a single electrode

To measure the heat of EDL formation for one type of counterion, measurements must be conducted at only one electrode. To this end, the electrodes between which current flows must be separated by several centimetres of solution to avoid measuring a combination of heat effects. In addition to expansion of the cell's dimensions, another modification is necessary, namely the inclusion of a reference electrode. The reference electrode is used to measure the potential of the electrode of interest, the working electrode. The inclusion of a reference electrode turns the cell into a three-electrode cell, as illustrated in Figure 11.

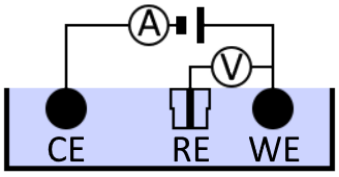

Figure 11: Schematic representation of a three-electrode cell. The power source is connected in series with an ammeter and a voltmeter is connected between the reference and working electrodes. WE: working electrode. CE: counter electrode. RE: reference electrode.

To determine the heat of EDL formation with a single ionic species as the counterion, the heat generated at the porous carbon working electrode must be measured, along with the flow of current between it and the counter electrode, as well as the applied potential vs. the reference electrode. The potential must be known to determine which ionic species is predominantly present in the EDL. The current must be known to determine the build-up of charge. Additionally, the current and potential data are both needed to determine the irreversible heat.

Because the measured heat is generated at only one electrode, one might expect to measure half the heat. This means the heat sensor must be at least twice as sensitive as the sensor used by *Janssen et al.* [7] Two different setups with two different, more sensitive sensors are developed in this work. One setup features four Pt100 resistance temperature detectors (RTDs) in a Wheatstone bridge as the heat sensor. The other setup features a *gSKIN®* thermocouple-based heat flux sensor. Both setups are described in detail below.

3.2 Temperature difference measurement setup

The temperature difference measurement setup, or RTD setup, consists of three components: an electrochemical cell, a box in which the temperature is carefully regulated and a Wheatstone bridge in which the resistors are thermometers. These components and the instruments to which they are connected will be treated separately.

The electrochemical cell is a three-electrode cell, in which the working electrode is a porous carbon disk (diameter 25 mm, thickness ca. 0.25 mm, weight ca. 82 mg) pressed against and glued to a non-porous carbon current collector with non-conductive *BISON KOMBI SNEL®* glue in a few spots; electrical contact was made mechanically using pressure from an O-ring seal. Previously, conductive silver epoxy glue was used, but this gave rise to unwanted electrochemical reactions. The counter electrode is a platinum coil and the reference electrode is an Ag/AgCl/sat. KCl electrode (+0.20 V vs. SHE). The working and counter electrodes are separated by ca. 5 cm of electrolyte solution. The reference electrode is located in a separate glass compartment, which is connected to the main body of the cell via a Luggin capillary, as in Figure 12. To apply a potential difference between the reference and working electrodes and to measure the current between the working and counter electrodes, a *Metrohm Autolab*

PGSTAT100 potentiostat is used.

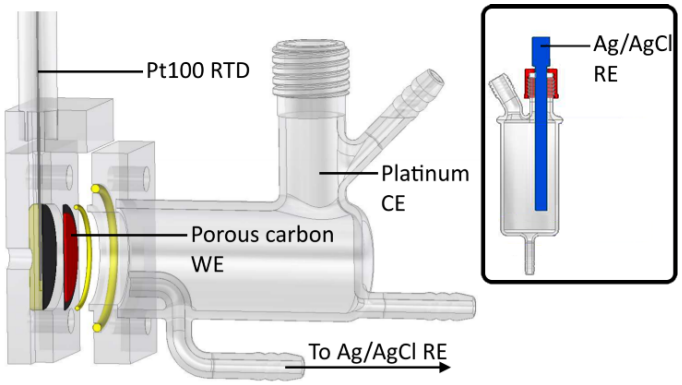

Figure 12: Isometric drawing of the interior of the RTD setup's electrochemical cell. Figure by H.J Siekman. Also see section 6.

To keep the temperature in the cell at a constant value, the main body of the cell is completely immersed in water in a large beaker, which is placed inside a thermostatted copper cylinder. This cylinder is built into a box that is connected to a water-filled *Julabo F25* thermostatic bath with a *Julabo HE* temperature control unit. The thermostatic bath pumps water into a compartment outside the copper cylinder. This water is kept at a constant temperature of 22 °C. The box itself is thermally insulated on all sides. See Figure 13 for an overview.

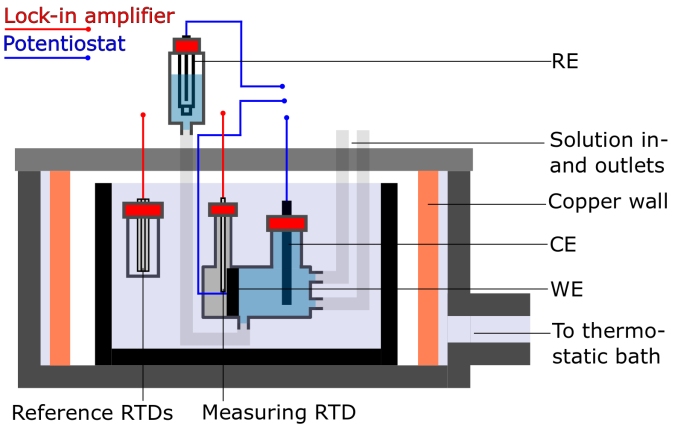

Figure 13: Schematic representation of the RTD setup. Not to scale.

Measurements of the temperature changes that occur during charging and discharging are performed using four thermometers in a Wheatstone bridge. Three of these are relatively insensitive and are used as reference thermometers, while the fourth thermometer is very sensitive and is capable of detecting temperature changes resulting from EDL charging and discharging. This more sensitive, very thin (0.5 mm thick) thermometer is positioned directly behind the working electrode and takes the place of the resistor R_M in the circuit shown in Figure 14. The bulkier, less responsive reference thermometers are the resistors R_e. They are located in their own separate compartment in the large beaker, as shown in Figure 13. All thermometers are Pt100 thermometers, which are *Resistance Temperature Detectors* (RTDs). They are resistors whose electrical resistance depends linearly on temperature, in the case of a Pt100 RTD following Equation 38, in which R has units of Ω and T has units of °C.

$$R = 100 + 0.385005T \tag{38}$$

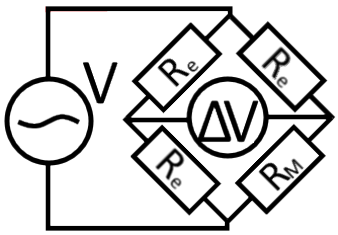

Figure 14: Wheatstone bridge circuit as used in the RTD setup.

When all thermometers are in an environment of equal temperature, the Wheatstone bridge should theoretically be balanced: there should be no voltage across the bridge. During experiments, an increase in temperature at the measuring thermometer leads to an increase in its electrical resistance and, consequently, to a non-zero voltage ΔV across the Wheatstone bridge. Both this voltage and the applied voltage are measured using a *Zürich Instruments HF2LI* lock-in amplifier, which is also used as the AC power source. It applies 500 mV at 100 kHz. To obtain the temperature difference between the measuring and reference thermometers, which are kept at constant temperature, Equation 39 is used. For a complete derivation, see Appendix I. In Equation 39, $\Delta R = R_M - R_e$, V is the applied voltage, and ΔV is the voltage across the Wheatstone bridge.

$$\Delta T = -\frac{1}{0.385005}\Delta R = -\frac{1}{0.385005}\frac{4\Delta V R_M}{V - 2\Delta V} \tag{39}$$

In practice, the temperature difference given by Equation 39 is non-zero when the setup is inactive. This is due to resistances elsewhere in the circuit. Appendix V (section 12.2) provides information about these resistances. The elevated ΔT baseline that results from the presence of these resistances is subtracted when integrating the data.

3.3 Integration of temperature difference and current data

The numerical integration of generic data $G(t)$ with respect to time is done step by step, following Equation 40. In this equation, there are N datapoints, n is an integer, and Δt is the time between two datapoints. Integration of both current data $I(t)$ and temperature data $\Delta T(t)$ is done following this equation.

$$\int_{t_0}^{t_1} G(t)\,\mathrm{d}t = \sum_{n=0}^{N} G(t + n\Delta t)\Delta t \tag{40}$$

In this work, it is necessary to modify the data before integration in two cases. Integration of temperature difference data can only be done after the baseline height has been subtracted. Similarly, integrating the current to determine the charge build-up requires any residual current to be subtracted. However, when current data are integrated to calculate Joule heating, the residual current is not subtracted.

Subtracting the residual current simply involves subtracting the value of the current in the last point of a current peak from all points in the peak. Subtracting the temperature difference baseline is more involved; there are three steps. First, an appropriate length of the peak $\tau_{\Delta T} = t_1 - t_0$ is chosen to avoid integrating too much noise. The chosen value for $\tau_{\Delta T}$ everywhere in this work is 1800 seconds. After determining $\tau_{\Delta T}$, the start of the ΔT peak t_0 is

visually identified. A line is fitted through the baseline from $t_0 - \tau_{\Delta T}$ to t_0 and another line is fitted through the baseline from $t_1 = t_0 + \tau_{\Delta T}$ to $t_0 + 2\tau_{\Delta T}$. The baseline between the ends of these lines is determined by linear interpolation, as is shown in Figure 15. It is subtracted from the ΔT signal during integration.

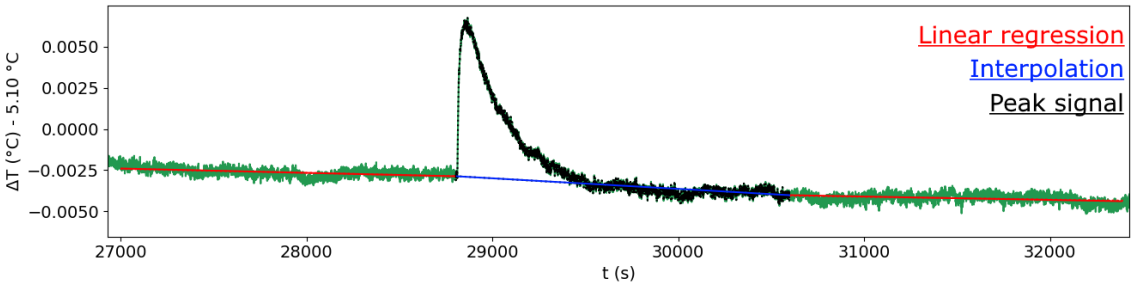

Figure 15: The integration procedure with baseline interpolation, applied to a single ΔT-peak.

The use of $\tau_{\Delta T} = 1800$ s to capture ΔT during charging and discharging introduces a deviation from the theory presented in section 2.5, in which a temperature difference peak ends where the next one begins. This means the peaks in a charge-discharge cycle are defined by three points in time: t_0, t_1 and t_2. However, with the procedure described in this section, the end of the temperature difference peak related to charging does not coincide with the start of the peak related to discharging, due to the use of a small $\tau_{\Delta T}$. This means there are actually two different t_1. This has consequences for the current integration. When a current peak is integrated to obtain the irreversible heat in the calibration step, it is integrated for the same length of time $\tau_{\Delta T}$ as the corresponding temperature difference peak. Therefore, the current data also features two different t_1. This is only true for the calculation of the irreversible heat. For determining the build-up of charge, the entire current peak is used.

3.4 Calibration of the temperature difference setup

Calibration of the temperature difference measurement setup is performed as described in section 2.5, by the procedure of *Janssen et al.* [7] The coefficient of heat transfer is used as a calibration constant. It is obtained via Equation 41.

$$\int_{t_0}^{t_2} I(t)\psi_R(t)\,\mathrm{d}t = K \int_{t_0}^{t_2} \Delta T(t)\,\mathrm{d}t \tag{41}$$

As mentioned in section 3.3, charge-discharge cycles do not last from t_0 to t_2, but consist of two $\Delta T(t)$-peaks and two corresponding $I(t)$-peaks of length $\tau_{\Delta T} = 1800$ s. Additionally, the current data $I(t)$ are affected by a constant residual current I_{res}, which is subtracted, as it is due to unwanted electrochemical reactions and not due to the build-up of charge. Residual current subtraction occurs in the calculation of ψ_R, Equation 42.

$$\psi_R(t) = \psi - \psi_C(t) = \psi - \frac{Q(t)}{C} = \psi\left[1 - \frac{\int_{t_0}^{t}(I(t') - I_{res})\,\mathrm{d}t'}{\int_{t_0}^{\infty}(I(t'') - I_{res})\,\mathrm{d}t''}\right] \tag{42}$$

3.5 Heat flux measurement setup

The second setup, which is still under construction, is built around a heat flux sensor (HFS), a device known to be capable of measuring tiny heat effects [8]. A heat flux sensor is made either of many thermocouples connected in series, or of a thermoelectric material. It responds directly to the flow of heat through its reactive area by building up a potential difference V, which can

be measured. The sensor in our setup is a *gSKIN®-XP269C* thermocouple-based heat flux sensor. Its dimensions are 10 mm × 10 mm × 0.5 mm.

The electrochemical cell used for heat flux measurements is similar to the temperature difference measurement cell, but the two cells are not identical. See Figure 16. The heat flux measurement cell is built to house a heat flux sensor and a copper heat sink instead of a thermometer. The only external compartment is the reference electrode compartment. The cell is designed to stand, as opposed to the cell for temperature difference measurements, which is designed to hang. To make the heat flux measurement cell more compact, the distance between the working and counter electrodes is smaller than in the temperature difference measurement cell.

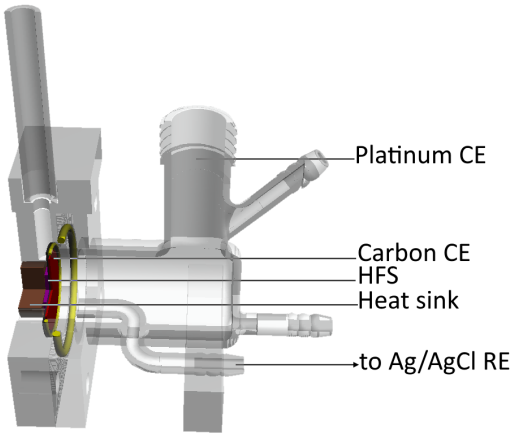

Figure 16: Isometric drawing of the electrochemical cell for heat flux measurements. Figure by H.J Siekman. Also see section 6.

To apply potentials and measure currents, a *PARSTAT MC1000* potentiostat is used. The signal from the heat flux sensor is recorded with a *Keithley 2182A* nanovoltmeter. The strategy for thermostatting the setup is still being worked on. One possible method is to place the cell in a beaker filled with water that is placed inside a thermostatic bath, as in Figure 17. Another possibility is the construction of a new, well-insulated box with water in- and outlets connected to a thermostatic bath. The cell could be placed at the heart of such a box. Ideally, the setup should be built to allow the temperature to stabilise at any desired value between 0 °C and 85 °C.

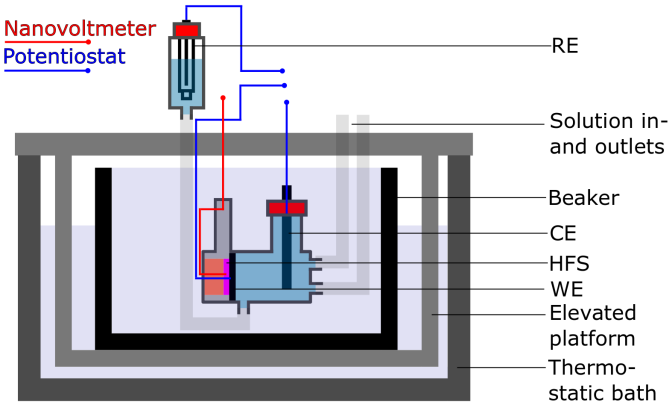

Figure 17: Schematic representation of one of the iterations of the setup for heat flux measurements. Not to scale.

3.6 Treatment of heat flux data

The integration of heat flux data follows exactly the same procedure as the integration of temperature difference data. The only difference is the name of the signal, which is $V(t)$ for the heat flux data. Just as the temperature difference baseline needs to be subtracted from the temperature difference data, the heat flux baseline must be subtracted from the heat flux data. Residual currents are also still a concern. They are dealt with as described in sections 3.3 and 3.4.

Calibrating the setup should be performed following the procedure in sections 2.5 and 3.4, although it must be noted that this has never actually been done for the HFS setup. Consequently, the appropriate length of a heat flux peak τ_V is unknown, but this can be established experimentally. Once it is established, it becomes possible to find the HFS setup's calibration constant k following Equation 43.

$$\int_{t_0}^{t_2} I(t)\psi_R(t)\,\mathrm{d}t = k\int_{t_0}^{t_2} V(t)\,\mathrm{d}t \tag{43}$$

3.7 Mapping the electrical and electrochemical behaviour of the system

We must know the potential of zero charge ψ_{zc}, also known as the equilibrium potential or the potential of zero current, in order to be able to charge and discharge the EDL fully. The potential of zero charge is determined by granting the entire cell several days to reach equilibrium in an *open circuit potential* measurement, during which no current can flow. Eventually, the potential reaches a plateau at ψ_{zc}, at which point the measurement is terminated. Because the potential tends to fluctuate somewhat, ψ_{zc} must be approximated.

Once ψ_{zc} has been determined, it must be verified that the capacitance is constant. Furthermore, any electrochemical phenomena that are unrelated to EDL formation must be identified. Both of these things are done by performing a *cyclic voltammetry* experiment, spanning the entire potential range of interest. In such an experiment, the applied potential is lowered from the most positive potential to the most negative potential, and then raised back to the most positive potential. The experiment may consist of multiple such cycles. During the whole experiment, the potential changes at a constant rate $\frac{\mathrm{d}V}{\mathrm{d}t}$.

In the case of this work, cyclic voltammetry experiments always consist of three cycles. The cycles are centred at ψ_{zc}. Cycles start at $\psi_{zc} + 0.5$ V, go down to $\psi_{zc} - 0.5$ V and then back up to $\psi_{zc} + 0.5$ V. A slow scan rate allows electrochemical reactions to be observed more clearly, which is why $\frac{dV}{dt} = 500\ \mu\mathrm{Vs}^{-1}$.

A constant capacitance can be readily identified if the current remains unchanged during the voltammetric experiment. This follows from Equation 44. Because the scan rate $\frac{\mathrm{d}V}{\mathrm{d}t}$ is constant, the current $I(t)$ should be constant if the capacitance C is also constant.

$$I(t) = \frac{\mathrm{d}Q}{\mathrm{d}t} = C\frac{\mathrm{d}V}{\mathrm{d}t} \tag{44}$$

Electrochemical reactions can be identified by looking for smooth peaks in the cycles. By scanning slowly, currents owing to reductions and oxidations become clearly visible against the small charging and discharging currents.

3.8 The typical chronoamperometric measurement

Combined chronoamperometric and calorimetric measurements are used to obtain the heat of EDL formation. The typical chronoamperometric measurement is a *voltage step* measurement.

In such a measurement, the zero current potential ψ_{zc} is applied for a time, after which the applied potential is changed to a non-equilibrium potential ψ^* for the same length of time. Then, ψ_{zc} is again applied for the same length of time. The EDL has now been charged and discharged. If the applied potential ψ^* is less than ψ_{zc}, the measurement is cathodic. Otherwise, it is anodic.

The measurement is continued by applying a new non-equilibrium potential ψ, which is closer to ψ_{zc} than the initial non-equilibrium potential ψ^* was. The potential is changed by the step change V. For a cathodic measurement, $\psi = \psi^* + V$, and for an anodic measurement, $\psi = \psi^* - V$. Once this new potential ψ has been applied for a sufficient length of time to charge the EDL, the EDL is discharged once more by setting the potential back to ψ_{zc} for the same length of time.

The procedure is repeated until $\psi = \psi_{zc} - V$ for a cathodic measurement or until $\psi = \psi_{zc} + V$ for an anodic measurement. V is chosen such that $(\psi^* - \psi_{zc}) \mod V = (\psi - \psi_{zc}) \mod V = 0$ for all ψ. See Table 1 for an example anodic measurement.

Potential (V)	**Duration (h)**
0.21	2
0.71	2
0.21	2
0.61	1.5
0.21	1.5
0.51	1
0.21	1
0.41	1
0.21	1
0.31	1
0.21	1

Table 1: Example anodic chronoamperometric measurement. The potential is the applied potential versus Ag/AgCl/sat. KCl.

The length of time during which a potential is applied depends on the potential. When the applied potential $\psi = \psi_{zc} + 0.50$ V or $\psi = \psi_{zc} - 0.50$ V, charging and discharging are given two hours to complete. When $\psi = \psi_{zc} + 0.40$ V or $\psi = \psi_{zc} - 0.40$ V, charging and discharging take $1\frac{1}{2}$ hours. At any other applied potential, charging and discharging take one hour.

The first cycle (0.71 V followed by 0.21 V in the example in Table 1) is recorded twice and the first attempt is discarded. This is to prevent any effects arising from changing from an anodic EDL to a cathodic EDL, or vice versa, from being incorporated. After all, the desired results are those that describe charging and discharging of one EDL, not the simultaneous discharging and charging of two different EDLs. Additonally, the surface chemistry of the porous carbon electrode may be affected by going from anodic to cathodic potentials or vice versa. Therefore, the first cycle serves to discharge the EDL of the previous measurement fully and to allow any necessary changes in surface chemistry to take place before continuing the measurement.

3.9 Acquisition and preparation of materials

The porous carbon material used in the working electrodes is provided by *Wetsus*. The material has a 1330 m^2g^{-1} specific surface area and a micropore volume of approximately 0.40 mLg^{-1} [7, 30]. Disks are cut out of this material and then glued onto a non-porous carbon disk using a small amount of *BISON KOMBI SNEL®* epoxy glue. The non-porous carbon is part of the current collector. The reference electrodes in both setups are pre-built *REF200* and *REF201* Ag/AgCl/KCl electrodes from *Radiometer Analytical*, with a saturated KCl solution inside. The

platinum counter electrodes are made by winding a coil of 2 m of platinum wire with a 0.2 mm diameter around a glass rod.

Solutions of 1 M NaCl and 0.8 M NaF in water are made by dissolving 58.68 g NaCl (*Merck*, analysis grade) and 16.76 g NaF (*Merck*, analysis grade) in 1 L and 0.5 L of *Milli-Q* water, respectively, followed by stirring. When a cell's solution is changed or refreshed, the cell is emptied, filled with *Milli-Q* water, emptied again, filled with the new solution, emptied once more and finally filled again.

3.10 Overview of conducted measurements

Measurement type	**Experimental details**	**N**
Open circuit potential	1 M NaCl; Lasted 64 h	1
Cyclic voltammetry	1 M NaCl; +0.71 V to −0.29 V; 500 μVs^{-1}; three cycles	1
Voltage step	1 M NaCl; +0.71 V to +0.21 V; steps of 0.10 V; RTD	5[a]
Voltage step	1 M NaCl; −0.29 V to +0.21 V; steps of 0.10 V; RTD	5[b]
Open circuit potential	0.8 M NaF; Lasted 120 h	1
Cyclic voltammetry	0.8 M NaF; +0.68 V to −0.32 V; 500 μVs^{-1}; three cycles	1
Voltage step	0.8 M NaF; +0.68 V to +0.18 V; steps of 0.10 V; RTD	2
Voltage step	0.8 M NaF; −0.32 V to +0.18 V; steps of 0.10 V; RTD	2

Table 2: All measurements conducted for this work.

a. One measurement did not feature a duplicate first cycle, but it was deemed safe to exclude it, as the previous measurement was also anodic.
b. One measurement was disrupted by an abrupt rise in ΔT in the middle of charging the EDL at −0.29 V. This particular charge-discharge cycle was discarded.

4 Results and discussion

4.1 Measuring small heat effects: capabilities of the RTD and HFS setups

To present the two setups' capabilities, a measurement result is shown for each. For the RTD setup, a typical measurement result looks like the lower plot in Figure 18. With the HFS setup, the result shown in Figure 19 has been obtained, although because the setup is still being worked on, the result cannot be called 'typical'.

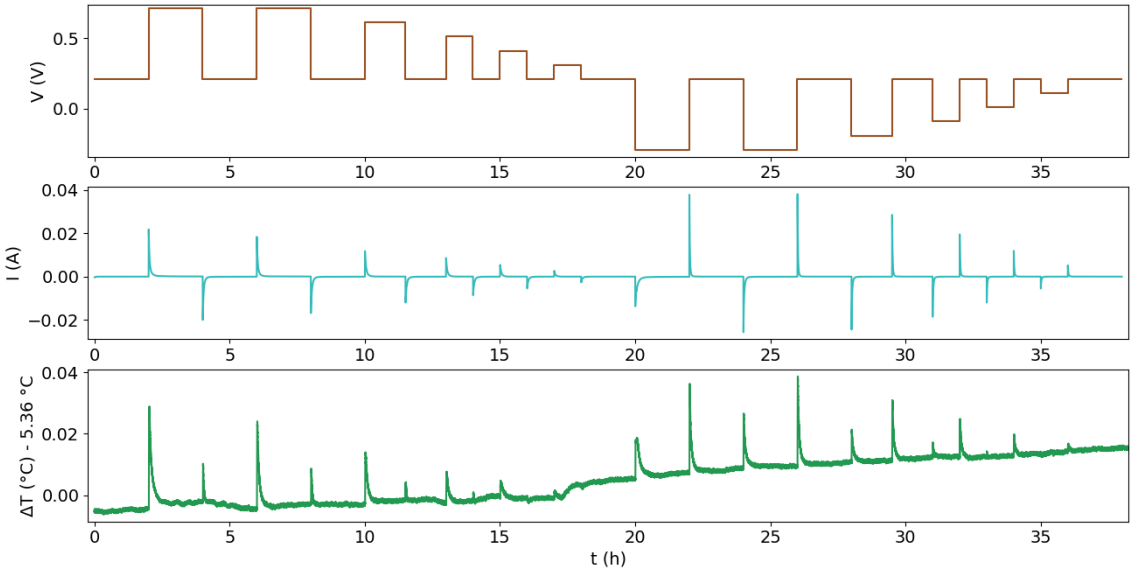

Figure 18: Temperature difference measurement with 1 M NaCl in the cell. The applied potential in the upper plot is vs. Ag/AgCl/sat. KCl. A constant value has been subtracted from the data in the lower plot to hide the effects of unwanted resistances in the Wheatstone bridge circuit.

There are clear shortcomings in the RTD result: the baseline is raised by ca. +5.36 °C and it continues to rise over time. Nevertheless, this result can easily be analysed using the methods described in sections 3.3 and 3.4. Peaks are visible for applied potentials from +0.5 V to +0.1 V vs. ψ_{zc} and from −0.5 V to −0.1 V vs. ψ_{zc}. Therefore, the reversible heat can be determined at all applied potentials.

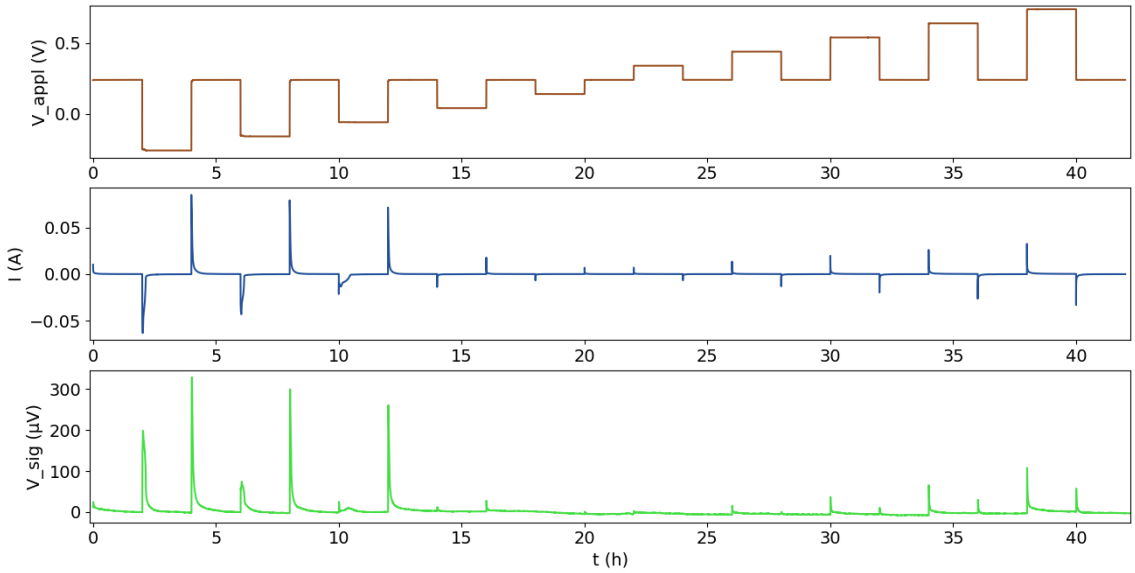

Figure 19: Heat flux measurement with 1 M NaCl in the cell. The applied potential in the upper plot is vs. Ag/AgCl/sat. KCl. The unusual shapes of the current peaks are due to the presence of a conductive, silver-containing glue in the system.

While the experiment that gave rise to Figure 19 is different from the one that led to Figure 18, it is still clear that the HFS setup can detect the same kind of heat effects that the RTD setup is designed to detect. Because the baseline of the heat flux sensor's signal is close to 0 V, subtracting the baseline is less important than it is for the RTD setup's ΔT signal. It may even be completely unnecessary.

While neither setup clearly out-performs the other in terms of heat detection, the HFS setup has a few advantages over the RTD setup. The HFS setup is more compact than the RTD setup, the circuitry involved is much simpler and there is no elevated baseline. Unfortunately, since the result in Figure 19 was obtained, technical difficulties have presented themselves. These difficulties have halted progress on the HFS setup for the duration of this project.

4.2 Determining the heat of EDL formation with 1 M NaCl using the RTD setup

4.2.1 The zero current potential

The first step towards determining the heat of EDL formation is the determination of the zero current potential ψ_{zc}. Figure 20 shows the result of the chronopotentiometric measurement from which ψ_{zc} can be determined for 1 M NaCl.

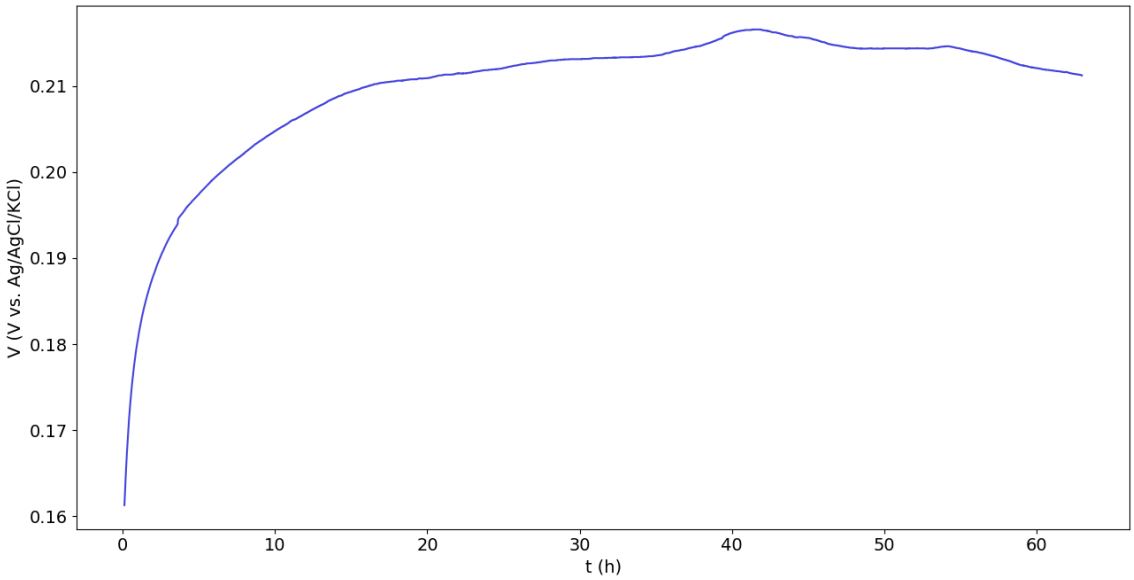

Figure 20: Measurement of the equilibrium open circuit potential ψ_{zc}.

After an initial rise, the potential stabilises around +0.21 V vs. Ag/AgCl/sat. KCl. This is the zero current potential ψ_{zc}. The fact that the potential took roughly 20 hours to reach this value, suggests that charged species enter and leave the electrode for a considerable length of time before equilibrium is reached.

4.2.2 Cyclic voltammetry

Now ψ_{zc} is known, a cyclic voltammogram is recorded to determine if the capacitance is constant and to map the electrochemical behaviour of the system. See Figure 21.

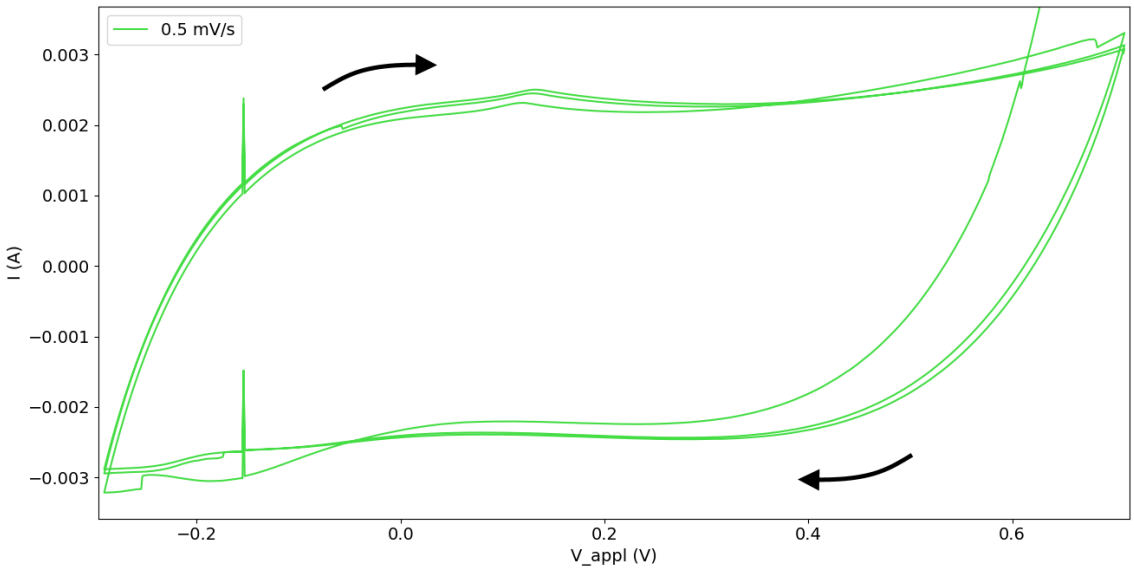

Figure 21: Cyclic voltammogram consisting of three cycles, from +0.71 V vs. Ag/AgCl/sat. KCl to −0.29 V vs. Ag/AgCl/sat. KCl and back, at 500 μVs^{-1}. Arrows indicate the scanning direction.

Between the changes in scanning direction, the current tends towards a plateau value, which indicates that the capacitance is constant across the entire potential range. While there are some irregularities in the cyclic voltammogram, there are no electrochemical reactions which can be clearly identified. This was once different: when the working electrode was attached to the current collector using silver-containing cold solder instead of non-conductive glue, an electrochemical reaction could be observed around 0 V vs. Ag/AgCl/sat. KCl, as in Figure 22. The peak at −0.1 V vs. Ag/AgCl/sat. KCl is due to the reduction of Ag^+ ions and the peak at +0.1 V vs. Ag/AgCl/sat. KCl is due to the oxidation of solid silver. The Ag(s)/Ag^+ redox couple is also central to the reference electrode, hence why the reaction can be observed around 0 V vs. Ag/AgCl/sat. KCl.

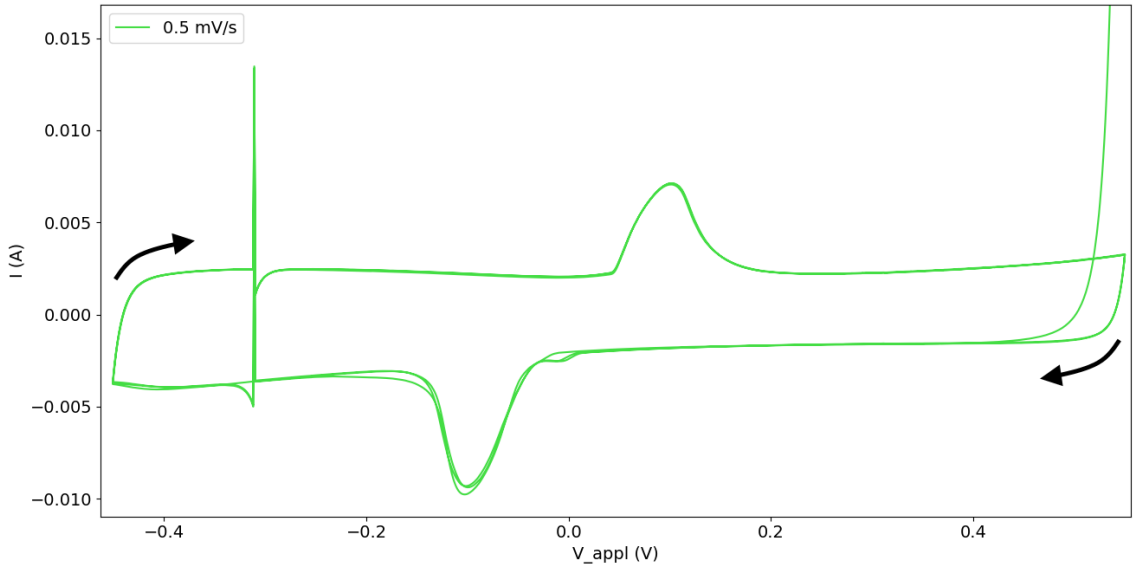

Figure 22: Cyclic voltammogram consisting of three cycles, from +0.55 V vs. Ag/AgCl/sat. KCl to −0.45 V vs. Ag/AgCl/sat. KCl and back, at 500 μVs^{-1}. Arrows indicate the scanning direction. This voltammogram was recorded before ψ_{zc} had been accurately determined and before the silver-containing epoxy glue had been eliminated from the system.

4.2.3 The heat of EDL formation

Finally, the heat of EDL formation is determined using the results obtained from the measurements listed in section 3.10. First, the data of all five measurements with 1 M NaCl are combined to calibrate the setup and obtain K. The calibration curve is shown in Figure 23. Then, K and the temperature difference data are used as described in sections 2.5 and 3.4 to calculate the irreversible heat and the reversible heat. These heats are plotted in Figure 24.

In all measurements, it is necessary to subtract residual currents following the procedure described in section 3.3. The cause of the residual currents is unknown, but it is hypothesised that the platinum counter electrode reacts with dissolved oxygen and with water, which results in the observed residual currents.

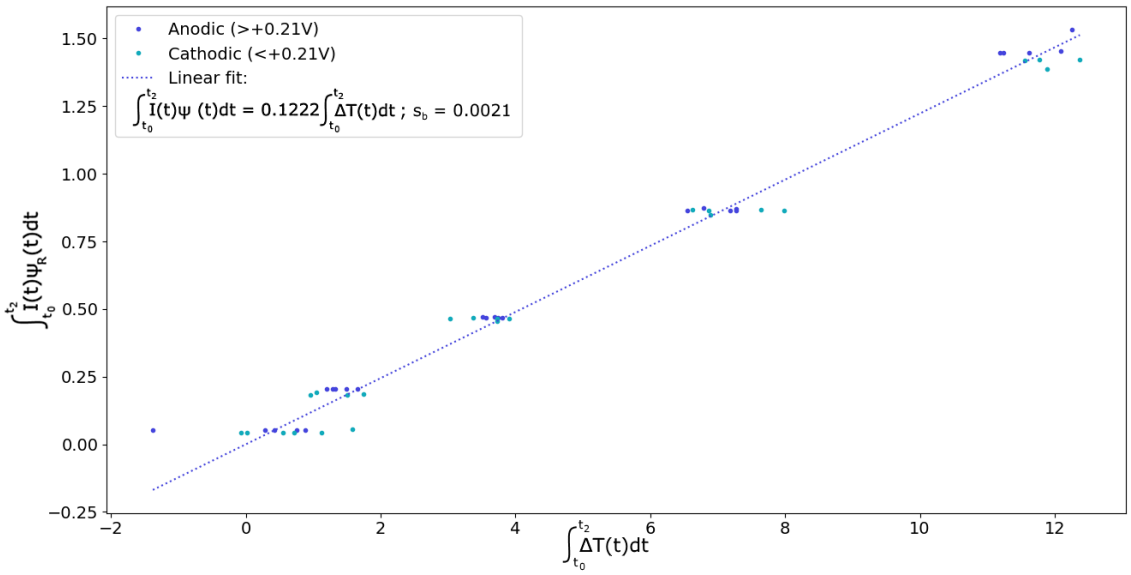

Figure 23: Calibration curve, obtained by using linear regression through the origin on the data of all measurements with 1 M NaCl. See Equation 35 for the origin of the axis labels. From linear regression, $K = 0.1222 \pm 0.0021$ JK^{-1}s^{-1}.

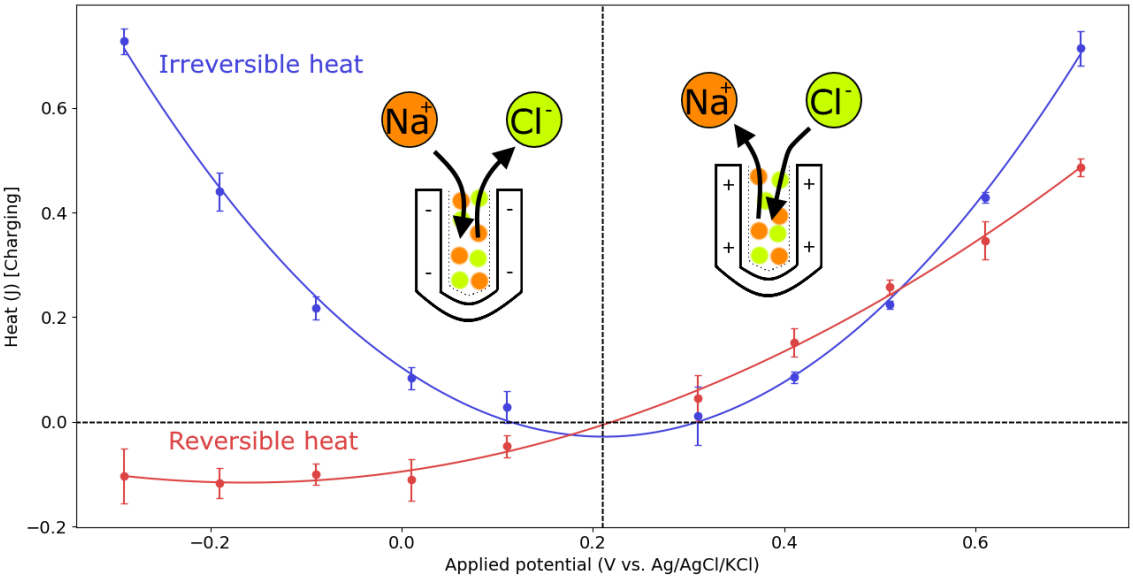

Figure 24: The reversible and irreversible heat for charging (or discharging) in 1 M NaCl. The dotted vertical line indicates ψ_{zc}.

The irreversible heat displays symmetry around $\psi_{zc} = +0.21$ V vs. Ag/AgCl/sat. KCl. This suggests that the current, accumulated charge and applied potential are the same in the anodic and cathodic regimes. Indeed, the applied potentials are exactly the same, except for the sign. The current peaks, however, are not of equal shape. When measuring cathodically, the sodium ions enter – and especially, leave – the electrode's pores more quickly than the chloride ions do when measuring anodically. This is visible in Figure 25. However, the accumulated charge is almost exactly the same, as is shown in Figure 26. As it turns out, the irreversible heat is also the same at cathodic and anodic potentials that are equally far removed from ψ_{zc}.

The trend in the reversible heat in Figure 24 is significantly different from the trend in the irreversible heat. The reversible heat steadily increases for chloride counterions (anodic), while it changes sign and remains nearly constant at all potentials for sodium counterions (cathodic). Some difference between the two ionic species has a major impact on the reversible heat. This will be further investigated in section 4.4.

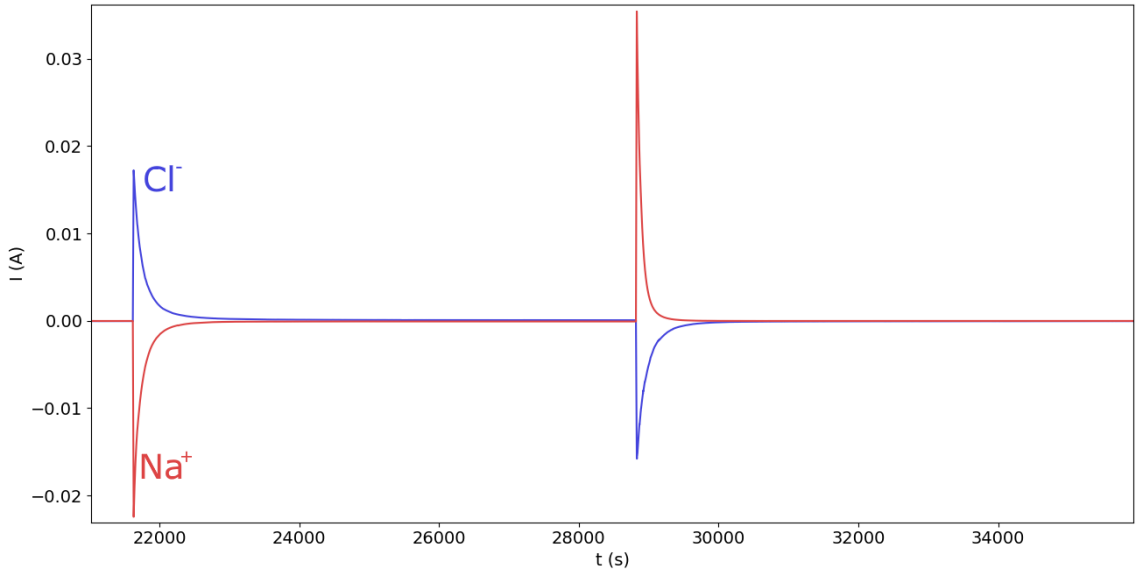

Figure 25: Typical current transients for 1 M NaCl at $V_{applied} = \psi_{zc} + 0.5$ V $= +0.71$ V (anodic, Cl^- counterions, blue) and at $V_{applied} = \psi_{zc} - 0.5$ V $= -0.29$ V (cathodic, Na^+ counterions, red). Taken from one anodic and one cathodic measurement.

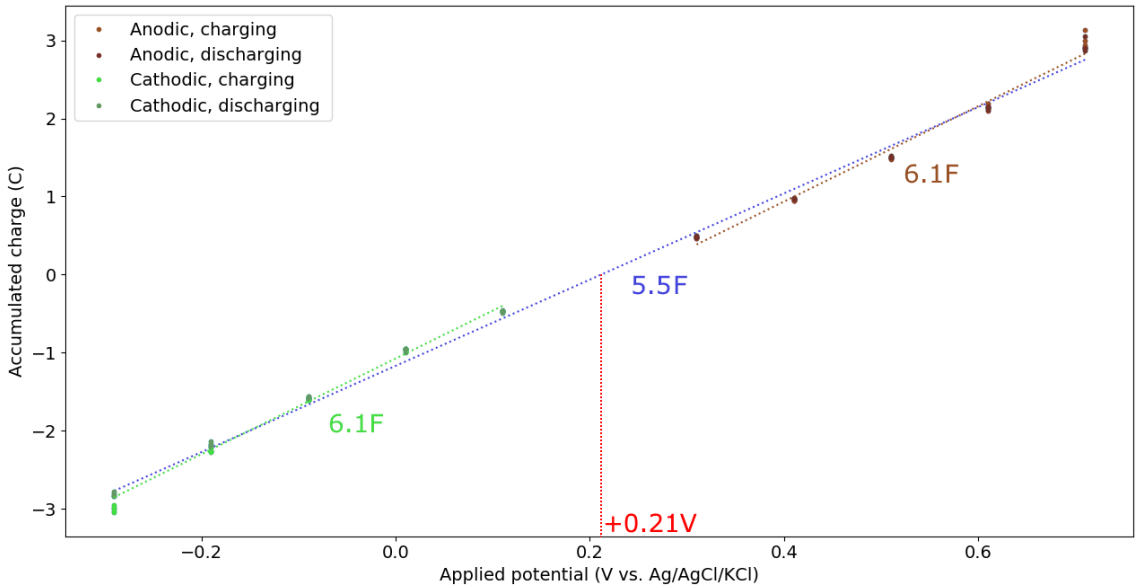

Figure 26: Capacitance of the electrode when the cell contains 1 M NaCl. The capacitance appears to be equal (6.1 F) for both Na^+ and Cl^- counterions.

4.3 Determining the heat of EDL formation with 0.8 M NaF using the RTD setup

4.3.1 The zero current potential

As with 1 M sodium chloride, the first step towards determining the heat of EDL formation for 0.8 M sodium fluoride is by determining ψ_{zc}. The measurement result shown in Figure 27 is used for this purpose.

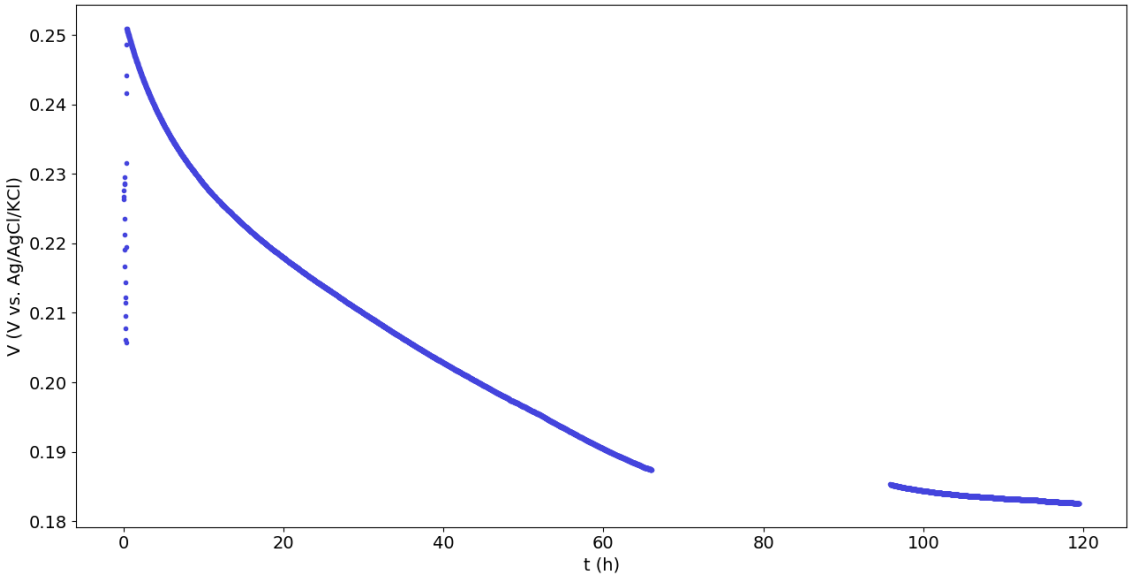

Figure 27: Measurement of the equilibrium open circuit potential ψ_{zc}. The gap in the curve is due to technical difficulties during the measurement.

The potential drops during the entire measurement, but after the interruption it levels off steadily, to about +0.18 V vs. Ag/AgCl/sat. KCl. This is the zero current potential ψ_{zc}.

4.3.2 Cyclic voltammetry

Now $\psi_{zc} = 0.18$ V has been found, a cyclic voltammogram is recorded. See Figure 28.

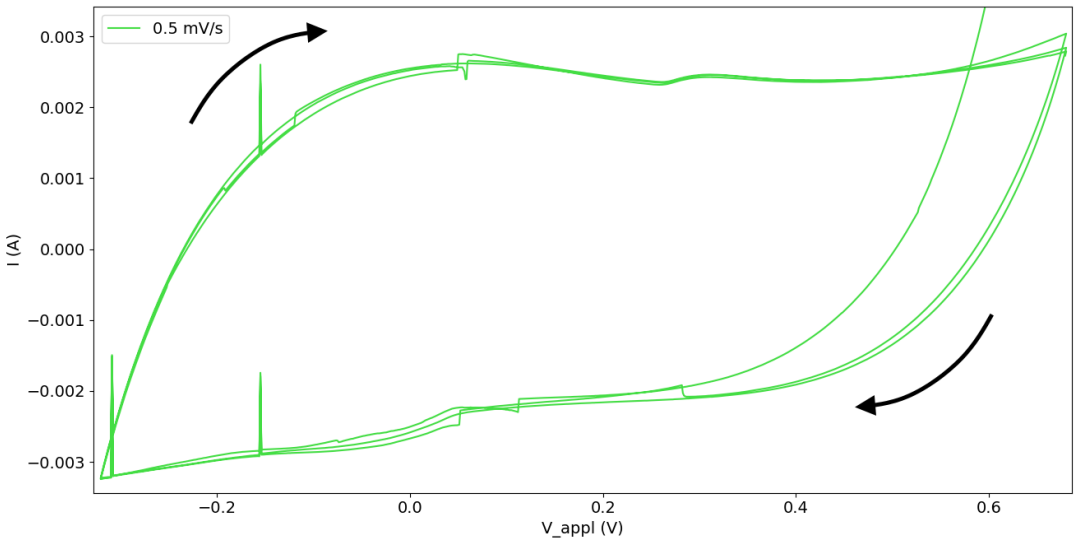

Figure 28: Cyclic voltammogram consisting of three cycles, from +0.68 V vs. Ag/AgCl/sat. KCl to −0.32 V vs. Ag/AgCl/sat. KCl and back, at 500 μVs^{-1}. Arrows indicate the scanning direction.

The current tends towards a plateau value throughout the potential range, with only minor deviations in the cathodic region. Therefore, the capacitance appears to be largely independent of the potential. There are no significant features in the voltammogram, which indicates that there are no major unwanted electrochemical reactions occurring in the system.

4.3.3 The heat of EDL formation

Calibration of the setup is performed again for 0.8 M NaF. The calibration constant obtained in section 4.2.3 is not used. See Figure 29 for the new calibration curve. Using the new coefficient of heat transfer, the heat of EDL formation is again determined and plotted in Figure 30.

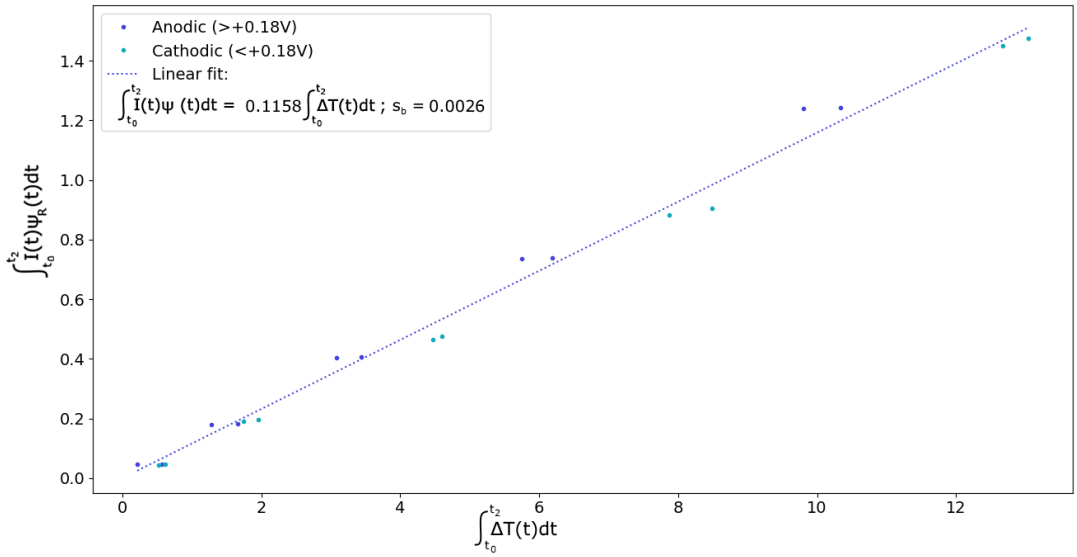

Figure 29: Calibration curve, obtained using linear regression through the origin on the data of both measurements with 0.8 M NaF. See Equation 35 for the origin of the axis labels. From linear regression, $K = 0.1158 \pm 0.0026$ JK^{-1}s^{-1}.

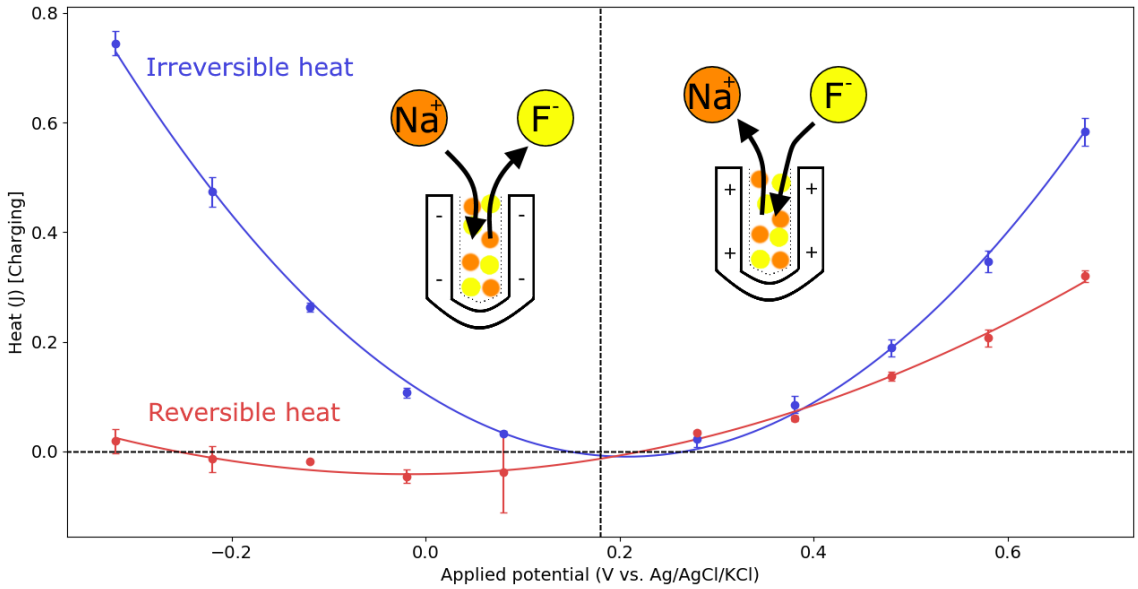

Figure 30: The reversible and irreversible heat for charging (or discharging) with 0.8 M NaF. The dotted vertical line indicates ψ_{zc}.

The reversible heat and irreversible heat follow different trends, as with 1 M NaCl. However, unlike the 1 M NaCl measurements, the 0.8 M NaF measurements show asymmetry with respect to ψ_{zc} in the irreversible heat as well. This can be explained by asymmetry in the build-up of charge, as is shown by the different anodic and cathodic capacitances in Figure 31.

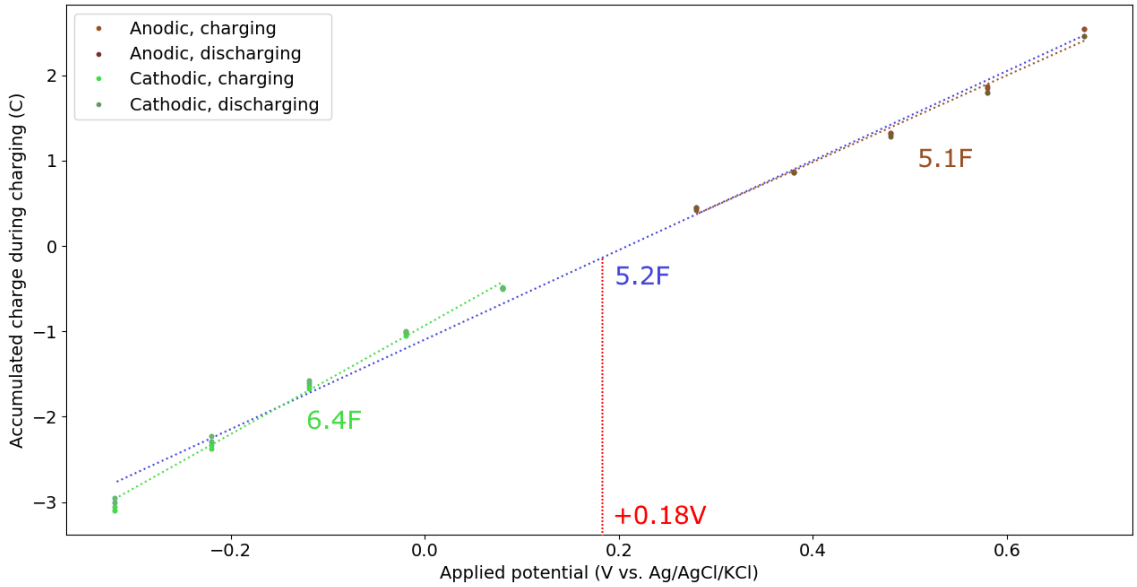

Figure 31: The capacitance with 0.8 M NaF. The capacitance is noticeably greater for Na^+ counterions (cathodic, 6.4 F) than for F^- counterions (anodic, 5.1 F).

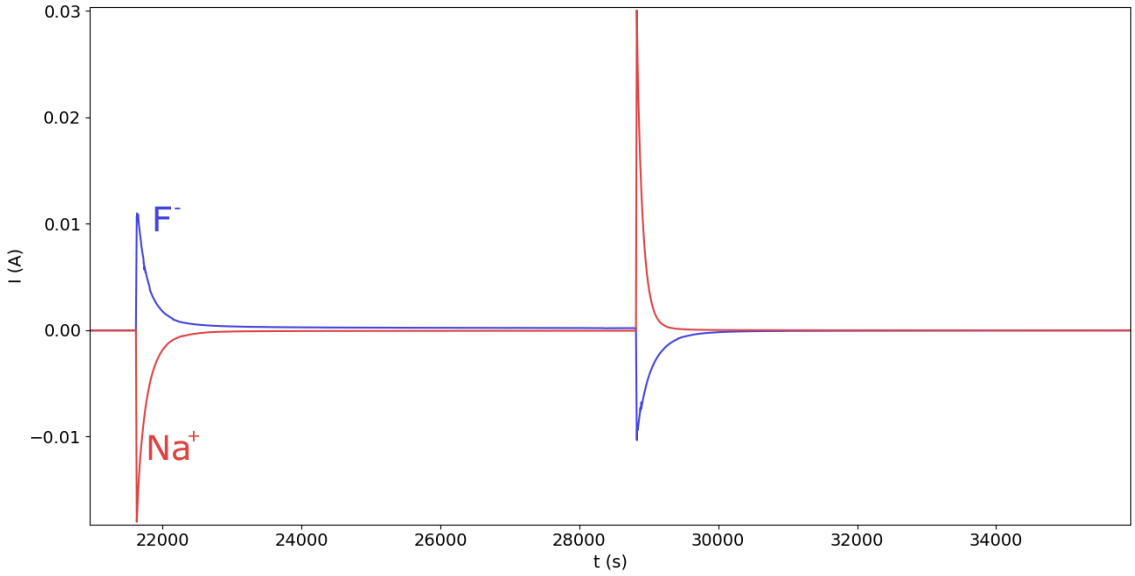

Figure 32: Typical current transients for 0.8 M NaF at $V_{applied} = \psi_{zc} + 0.5$ V $= +0.68$ V (anodic, F^- counterions, blue) and at $V_{applied} = \psi_{zc} - 0.5$ V $= -0.32$ V (cathodic, Na^+ counterions, red). Taken from one anodic and one cathodic measurement.

Figure 31 shows that more sodium than fluoride can enter the electrode at the same distance from ψ_{zc}, while Figure 32 shows that sodium ions also enter the electrode's pores *more quickly*. Due to the differences in the total accumulated charge and the rate of charge build-up, the irreversible heat generated while the counterions are Na^+ ions is greater than the irreversible heat observed with F^- counterions.

The reversible heat, however, is much higher for F^- counterions, despite fewer ions being involved. This is similar to the result observed for 1 M NaCl, in which EDLs with chloride counterions give rise to far greater reversible heat, despite the number of ions involved being (nearly) equal to the number of sodium ions in an EDL with those as the counterions. In both the 0.8 M NaF and 1 M NaCl cases, the anions appear to differ from Na^+ in such a way that they completely dominate the reversible heat.

4.4 Towards explaining the heat of EDL formation

In an effort to explain why fluoride and chloride counterions give rise to a much greater heat of EDL formation than sodium counterions, an attempt is made to formulate a model that can account for the asymmetry in the reversible heat as a function of the potential, as observed for both 0.8 M NaF and 1 M NaCl in Figure 33. This model is kept relatively simple, in view of the limited time still available to finish the project.

The heat of EDL formation could have both enthalpic and entropic origins. Enthalpic changes should be due to, possibly amongst others, the field energy and the hydration of the ions, while entropic changes should be influenced by the ionic radii. These three contributing factors are investigated in their own sections.

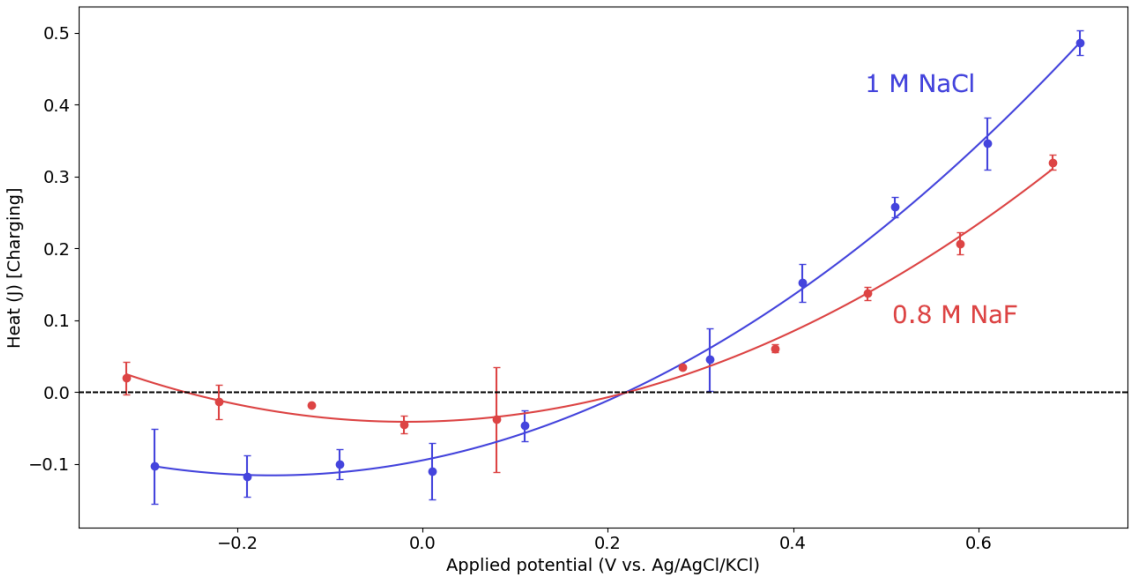

Figure 33: Heats of EDL formation. Note the asymmetry with respect to ψ_{zc} (+0.21 V for 1 M NaCl and +0.18 V for 0.8 M NaF, vs. Ag/AgCl/sat. KCl).

4.4.1 Field energy

As mentioned in section 2.4, the field energy is negligible if the Debye screening length far exceeds the pore diameter. The Debye screening length κ^{-1} follows from Equation 45 for a 1:1-electrolyte of concentration n_0 in units of molm^{-3}.

$$\kappa^{-1} = \sqrt{\frac{\epsilon_r \epsilon_0 kT}{2e^2 N_{Av} n_0}} \tag{45}$$

The porous carbon material used in this work has an average pore diameter of approximately 1 nm. For 1 M NaCl, the Debye screening length is roughly 0.30 nm, while for 0.8 M NaF, the Debye screening length is 0.34 nm. In both cases, the Debye screening length at $T = 295$ K is less than the pore size. Therefore, the field energy cannot be out-right neglected if the bulk concentration is used to calculate the Debye screening length.

While this suggests that the field energy must be considered, there is experimental evidence for the heat of EDL formation being practically independent of concentration and, consequently, independent of the Debye screening length. Measurements by *Janssen et al.* [7] reveal that the electrolyte concentration only has a minute effect on the heat of EDL formation. By extension, the Debye screening length appears to be of little consequence. See Figure 34.

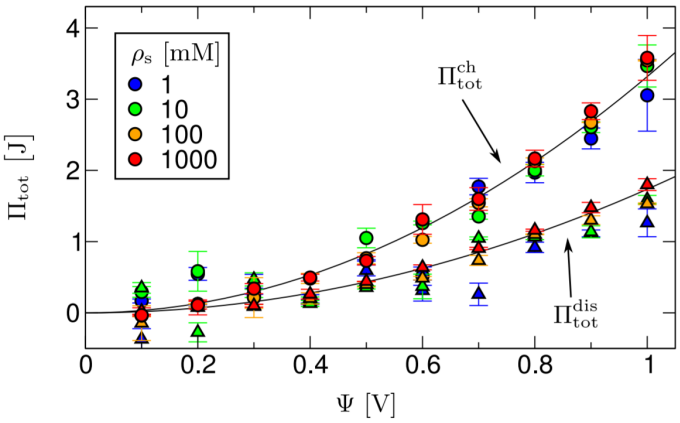

Figure 34: The total heat during charging and discharging at different cell voltages, as found by *Janssen et al.* [7] for a compact two-electrode cell. Figure taken from *Janssen et al.* [7]

It is possible that the field energy still plays a part in the heat of EDL formation, but with experimental evidence to the contrary, the field energy shall not be considered after this section.

4.4.2 Hydration

The enthalpy of hydration ΔH^0_{hyd} is the enthalpy change when a gaseous ion is dissolved in an infinitely large volume of water [31]. When an ion is dissolved, it is hydrated by water molecules, which form a hydration shell around the ion. For such a hydration shell to be affected by EDL charging, the heat of EDL formation should at least be comparable to the enthalpy of hydration divided by the number of water molecules in the hydration shell.

Hydration enthalpies are given for Na^+, Cl^- and F^- in Table 3. Conceivably, there may be interactions in the system which stabilise water molecules after dehydration, thereby reducing the enthalpy change to less than ΔH^0_{hyd} divided by the number of coordinated water molecules. Such interactions are not accounted for in the definition of ΔH^0_{hyd}, because this definition assumes an infinite amount of water, whereas in our case, the amount of water is finite. Additionally, ions could be stabilised after partial dehydration by adsorbing to the oppositely charged electrode. This would further decrease the required heat for dehydration.

Ionic species	$\mathbf{\Delta H^0_{hyd}/6}$ **(kJmol^{-1})**
Na^+	68.2
Cl^-	63.5
F^-	85.8

Table 3: Hydration enthalpies of all ionic species considered in this work, divided by six, the number of coordinated water molecules [31]

.

However, while these stabilising interactions may exist, it is important to realise just how large the values for ΔH^0_{hyd} in Table 3 are. The lowest value of $\Delta H^0_{hyd}/6$, 63.5 kJmol^{-1}, belongs to chloride. While it is the lowest value in the table, it is still higher than the evaporation enthalpy of water, which is 40.5 kJmol^{-1} [32]. As such, the hydration enthalpy per water molecule is greater than the heat required to completely tear a water molecule out of the solution.

It seems reasonable to assume that any interactions that could stabilise the ions or the water molecules would not exceed the evaporation enthalpy. While this is more of a guess than a

substantiated assumption, it does allow a simple rule to be formulated for dehydration: for one of the six bound water molecules to leave the hydration shell of an ion during EDL charging, the heat of EDL formation must *at least* exceed $\frac{1}{6}^{th}$ of the hydration enthalpy minus the evaporation enthalpy of water. For Cl^-, the least heat is required: 23.5 $kJmol^{-1}$. The measured heat is substantially less than that, as is shown in Figure 35.

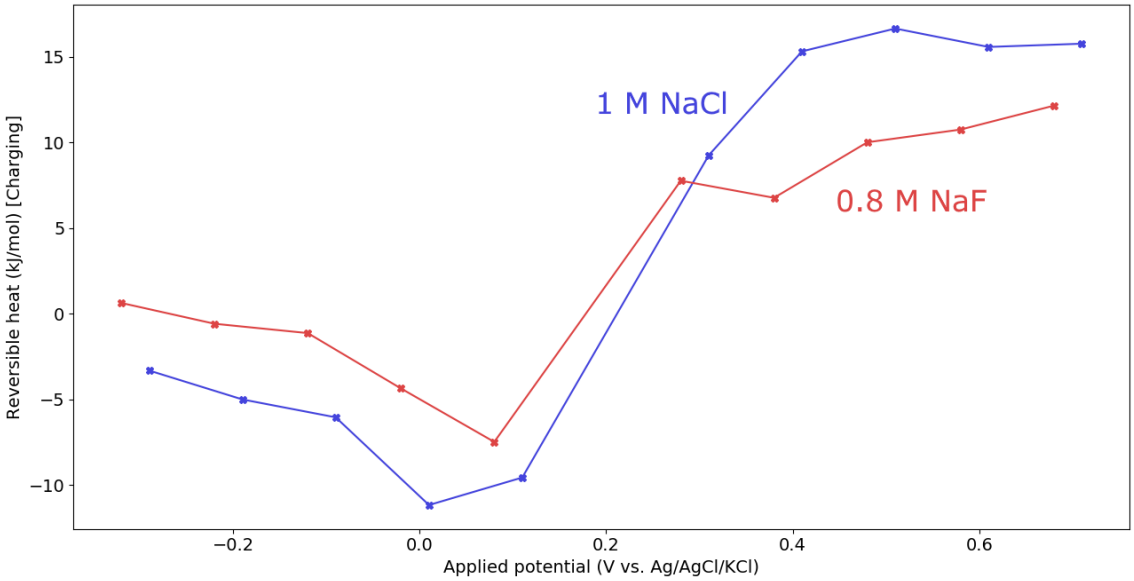

Figure 35: The reversible heat per mole of moved ions. The reversible heat (Figure 33) was divided by $Q_{charging}/F$ to give the reversible heat per mole of moved ions.

Figure 35 shows that the reversible heat per mole of moved ions is insufficient to account for any dehydration of the ions. The reversible heat does not exceed 16 $kJmol^{-1}$, while at least 23.5 $kJmol^{-1}$ would be necessary for partial dehydration of the chloride ions according to our – admittedly rather arbitrary – rule. Therefore, hydration cannot be considered a factor in the heat of EDL formation, just like the field energy. Ions remain fully hydrated, which is consistent with the Stern layer picture of the EDL, where the ions are separated from the electrode by a layer of water molecules. With both enthalpic contributions disqualified, this leaves only entropic effects as a possible explanation of the heat of EDL formation.

4.4.3 Ionic radii

The most promising explanation of the asymmetry in the heat of EDL formation lies in the entropic change that occurs upon charging and discharging of the EDL. The different types of ions have different ionic radii, and thus they occupy different volume fractions at the same concentration. This leads to less freedom of movement (less entropy) for large ions than for small ones when the ions are confined to a small volume, such as a pore.

When an EDL is charged, ions are exchanged. In the case of large anions and small cations, applying a positive, anodic potential causes more large anions to enter the pores, while small cations leave. The entropy is thus reduced. Applying a negative, cathodic potential has the opposite effect, as is shown in Figure 36. These effects can be captured in a model using a definition for entropy that accounts for the ionic radii. The model that we use is described in the remainder of this section.

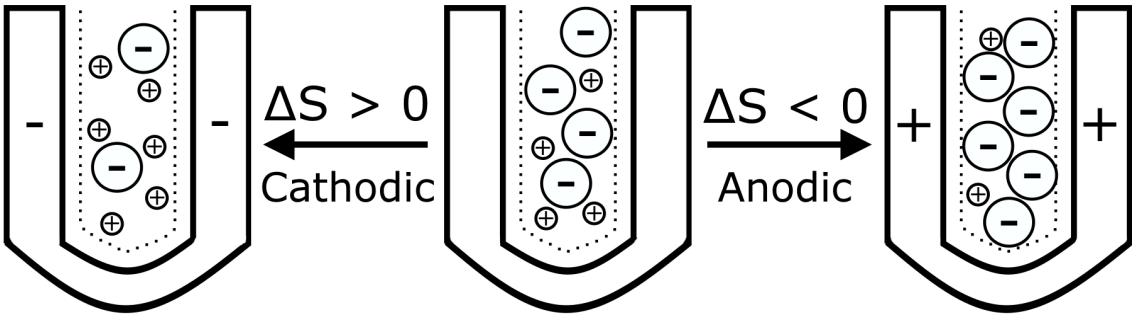

Figure 36: Illustration of the essential concept behind the exclusively entropic model.

In the model for the entropic effect, henceforth the *exclusively entropic model*, the pores and the bulk solution are assumed to be in equilbrium: $\mu_+^{pores} = \mu_+^{bulk}$ and $\mu_-^{pores} = \mu_-^{bulk}$. This results in a constant ionic product $n_0^2 = n_+ n_-$. Electroneutrality is also assumed. Furthermore, one capacitance C is assumed for all ionic species.

Given that the porous carbon is capable of bearing an electric charge, the electroneutrality condition is:

$$n_+ - n_- + z n_s = 0 \tag{46}$$

In Equation 46, $z = -1$ for anodic potentials and $z = +1$ for cathodic potentials. The concentration of surface charges n_s follows from the capacitance C, the applied potential ψ and the micropore volume V via Equation 47.

$$n_s = \frac{C\psi}{FV} \tag{47}$$

In this equation, $\psi = V_{applied} - \psi_{zc}$. Now, by defining $n_0^2 = n_+ n_-$ and realising that $z n_s = \psi n_0$, we can relate the surface charge to the applied potential and the ions' concentrations:

$$n_0^2 = n_+(n_+ + \psi n_s) \tag{48}$$

This results in a simple quadratic equation:

$$n_+^2 + \psi n_s n_+ - n_0^2 = 0 \tag{49}$$

Solving for the cation concentration gives:

$$n_+ = \frac{1}{2}\left(\sqrt{4n_0^2 + n_s^2} - n_s\right) \tag{50}$$

The anion concentration simply follows from $n_- = n_+ + n_s$.

The concentrations of the ions are needed to determine the heat $T\Delta S$. To do so, Equation 51 is used for the entropy S. This equation describes the entropy as a mixing entropy of spheres of different sizes [33].

$$S = -k\big[N_w \ln \phi_w + N_+ \ln \phi_+ + N_- \ln \phi_-\big] \tag{51}$$

In this equation, the ionic species' volume fractions ϕ_+ and ϕ_- follow from Equation 52, which features the ionic concentrations $n_\pm$, volumes $v_\pm$ and radii $r_\pm$.

$$\phi_\pm = n_\pm N_{Av} v_\pm = n_\pm N_{Av} \frac{\pi(2r_\pm)^3}{6} \tag{52}$$

The water, lastly, has a volume fraction $\phi_w = 1 - \phi_+ - \phi_-$. The amounts of ions N_+ and N_- and the amount of water N_w can be determined in a straightforward manner, following Equations 53 and 54, in which V is the micropore volume. The water concentration n_w can be determined from the molar volume of liquid water, $18 mL mol^{-1}$.

$$N_\pm = V n_\pm N_{Av} \tag{53}$$

$$N_w = V n_w N_{Av} \tag{54}$$

With the entropy defined and all variables explained, it is time to return to the heat of EDL formation. The entropic contribution to the heat of EDL formation is $T\Delta S$, the difference between the entropy at an applied potential ψ and at the zero current potential ψ_{zc}.

$$T\Delta S = T\big(S(\psi) - S(\psi_{zc})\big) \tag{55}$$

If entropic effects are solely responsible for the heat of EDL formation, Equation 55 is the expected measurement result. To assess the viability of the model, the model and the experimental data are compared in Figure 37.

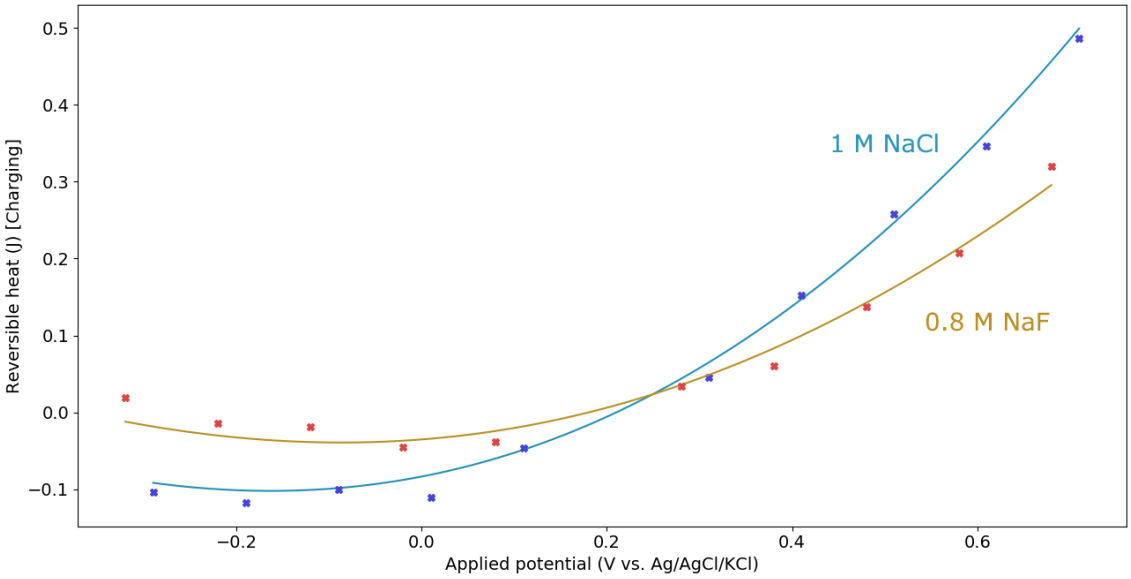

Figure 37: The model (lines, translated to ψ_{zc}) compared to experimental data (cross markers). Parameters: $r_{Na^+} = 350$ pm; $r_{Cl^-} = 435$ pm; $r_{F^-} = 415$ pm; $C_{NaCl} = 6$ F; $C_{NaF} = 5$ F; $V = 38$ μL.

The parameters used to create the near-perfect fit in Figure 37 are not entirely representative of the system, but the chosen values are not physically implausible. The primary objection to the fit is the choice of ionic radii, which differ from literature values [30, 34]. The literature values for the ions are $r_{Na^+} = 358$ pm, $r_{Cl^-} = 332$ pm and $r_{F^-} = 352$ pm [34]. While a deviation from the literature values is not necessarily problematic, it is curious to see that our model works when Cl^- and F^- are larger than Na^+, which is the opposite of generally accepted reality. However, even this is not necessarily problematic, because the literature values are determined using conductivity measurements, from which hydrodynamic radii are obtained [35]. A hydrodynamic radius obtained via a conductivity measurement is unlikely to be an appropriate indication of the size of an ion in porous carbon, where the assumption that a hydrated ion is simply a free-floating sphere does not necessarily hold.

There is also a slight deviation from the literature value of the micropore volume (475 $\mathrm{mLg^{-1}}$ in our case vs. 400 $\mathrm{mLg^{-1}}$ in literature) [30]. This is not necessarily problematic, as the deviation is not very large and the literature value was determined using nitrogen adsorption. A micropore volume obtained via nitrogen adsorption is not necessarily representative of the ion-accessible volume, which is the volume that matters in this model.

All in all, despite its shortcomings, the model is clearly capable of producing the correct trend, which is encouraging. This model for the entropic heat generation should definitely be further developed. One way to improve it would be to use the excluded volume instead of the occupied volume of the ions [26]. This would involve a different expression for the entropy, such as the entropy of hard sphere ions, which can be calculated using the mean-field formalism [36]. By treating the ions as hard sphere ions, correlations between the ions can be accounted for. This is probably necessary, as our current model predicts ionic volume fractions as high as 30% for $\mathrm{Cl^-}$ ions in 1 M NaCl at applied potentials around +0.71 V vs. Ag/AgCl/sat. KCl.

Another reason to change the expression for the entropy is the predicted concentration dependence of the result. Experimental results from *Janssen et al.* [7] indicate that the heat of EDL formation is practically independent of concentration, as shown in Figure 34. Consequently, the predicted entropy change should also be independent of the concentration. This is not the case, however, as Figure 38 shows.

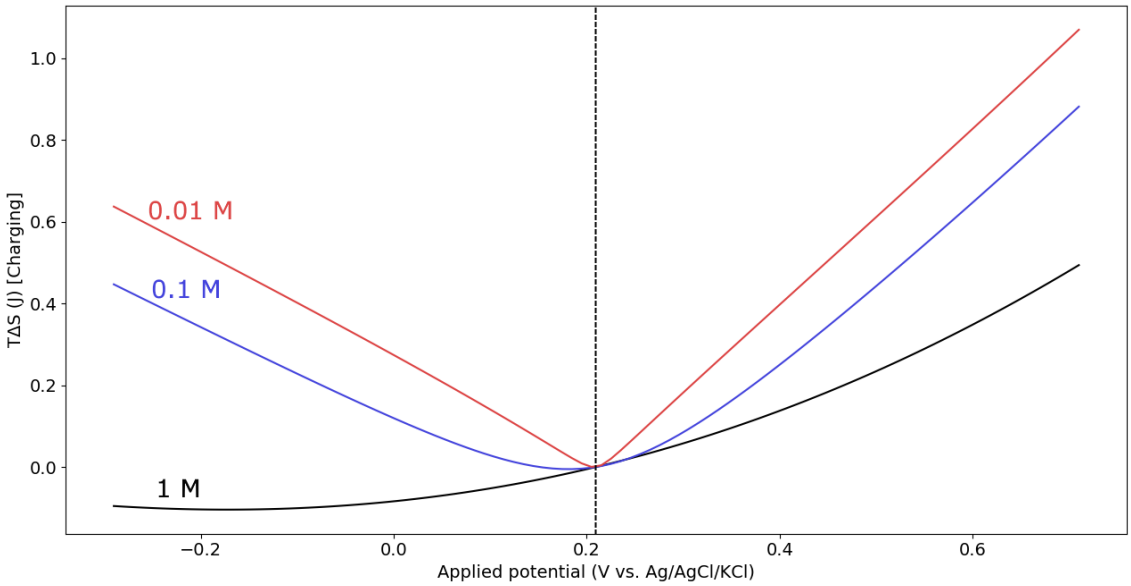

Figure 38: Concentration dependence of the exclusively entropic model, using the parameters used for NaCl in Figure 37. The dotted vertical line indicates ψ_{zc}.

Finally, a possible improvement that does not require a different expression for the entropy, is to use two capacitances C_+ and C_- for the cations and the anions respectively, instead of using one capacitance C for both. This would be especially helpful for NaF, as the electrode's capacitance for $\mathrm{F^-}$ is significantly smaller than its capacitance for $\mathrm{Na^+}$.

5 Conclusions and outlook

With the temperature difference measurement setup, it is possible to measure the reversible heat of EDL charging in porous carbon over a range of voltages, from an applied voltage that is 0.5 V more positive or negative than the equilibrium potential down to one that is only 0.1 V more positive or negative. As a result, the heat of electrical double layer formation can be determined as a function of the applied potential for chloride, fluoride and sodium counterions.

There is asymmetry in the heat of EDL formation as a function of the applied potential, both for 1 M NaCl and for 0.8 M NaF. The heat of EDL formation is much greater with Cl^- and F^- counterions than with Na^+ counterions. This is likely due to differences in the ionic radii, which lead to vastly different entropic changes and different EDL formation heats. Enthalpic changes appear to be less important, as dehydration is unlikely to occur with as little heat as is measured. Additionally, the electric field energy is likely very small [28].

As a result of the seemingly negligible enthalpy, a simple, exclusively entropic model for the heat of EDL formation works quite well to explain the experimental results. The model takes the ionic radii and the micropore volume into account. Although using literature values for the ionic radii does not result in a quantitative fit, the model is capable of reproducing the experimental data using ionic radii that are at least physically plausible.

Future developments in this line of research will focus on improving the model, for example by considering one capacitance for each ionic species, instead of one capacitance for the two-component electrolyte. Considering the high ionic volume fractions predicted by the model, it is likely also justified to change the expression for entropy to account for correlations between the ions' positions. Finally, other models will be tested, such as the existing modified Donnan model by *Porada et al.* [28], which could be expanded to allow the enthalpy and entropy to be calculated.

Experimental work will continue by investigating different ionic species. If ionic radii matter as much as this work suggests, the relatively large Li^+ ions and the relatively small K^+ ions should be worth looking into. Divalent ions could also be interesting, provided that a suitable 2:2- or 2:1-electrolyte can be found. A 2:2-electrolyte is preferable if the number of moved ions is to be calculated. It could also be useful to attempt to work with the ionic species that have already been investigated, but at lower electrolyte concentrations, as this would increase the Debye screening length. This should suppress the influence of the – presumably already tiny – electric field energy on the heat of EDL formation. Lowering the electrolyte concentration would also put the exclusively entropic model, which predicts significant concentration dependence of the reversible heat, to the test.

Finally, two new types of measurements will be attempted. To learn more about the accumulation of ions in porous carbon, NMR measurements will be conducted at the same time as charge measurements, which should provide information about the co- and counterion concentrations in the porous carbon. This would, for example, allow one to find out if fluoride indeed enters the electrode in smaller amounts than sodium or chloride.

The other new type of measurement is one in which the heat of EDL formation is determined at different temperatures. This should allow the separation of the enthalpic and entropic contributions to the heat of EDL formation.

6 Acknowledgements

This thesis could not have been written without the support of the students and staff of the Van 't Hoff Laboratory for Physical and Colloid Chemistry, as well as a few other contributors. There are several people whom I would especially like to thank.

I am grateful for the excellent supervision from Dr. Ben Erné and Joren Vos. They have both provided excellent guidance and feedback. Additionally, Ben has made large contributions to the project, particularly to the construction of the setups and to the development of methods and theory. The model in section 4.4 is entirely Ben's work. Joren has also contributed much to the setups, as well as the measurements conducted with them. His help with all kinds of practical matters relating to the measurements is gratefully acknowledged.

Furthermore, I would like to thank Bonny Kuipers for helping us select the appropriate instruments for the temperature difference measurement setup and for protecting this setup and other equipment against voltage spikes. For the latter, I would also like to thank Dr. Dominique Thies-Weesie. The work of Henkjan Siekman, who designed and built the electrochemical cells, is also gratefully acknowledged. Lastly, I would like to thank Ties Bakker for his excellent work on the development of the heat flux measurement setup.

I would also like to thank Prof. Albert Philipse for helpful discussions and for acting as the second examiner for my work. Lastly, I would like to thank Raimon Terricabres for his help with one of the experiments and Iwan Haensel for helpful discussions.

The efforts of *Wetsus* to supply us with porous carbon are gratefully acknowledged.

This master's project is part of the larger research programme "Experimental Thermodynamics of Ion Confinement in Porous Carbon Electrodes", with project number NWO-ECHO 712.018.001, which is financed by the Dutch Research Council (NWO).

7 References

(1) Wall, S. *Curr. Opin. Colloid Interface Sci.* **2010**, *15*, 119–124.

(2) Porada, S.; Zhao, R.; van der Wal, A.; Presser, V.; Biesheuvel, P. *Prog. Mater. Sci.* **2013**, *58*, 1388–1442.

(3) Goh, P.; Ismail, A. *Desalination* **2018**, *434*, Reviews on Research and Development in Desalination, 60–80.

(4) Zhao, R.; Biesheuvel, P.; Miedema, H.; Bruning, H.; van der Wal, A. *J. Phys. Chem. Lett.* **2010**, *1*, 205–210.

(5) Brogioli, D.; Zhao, R.; Biesheuvel, P. M. *Energy Environ. Sci.* **2011**, *4*, 772–777.

(6) Schiffer, J.; Linzen, D.; Sauer, D. U. *J. Power Sources* **2006**, *160*, 765–772.

(7) Janssen, M.; Griffioen, E.; Biesheuvel, M.; Roij, R.; Erné, B. *Phys. Rev. Lett.* **2017**, *119*, 166002.

(8) Munteshari, O.; Lau, J.; Krishnan, A.; Dunn, B.; Pilon, L. *J. Power Sources* **2018**, *374*, 257–268.

(9) Etzel, K. D.; Bickel, K. R.; Schuster, R. *Rev. Sci. Instrum.* **2010**, *81*, 034101.

(10) d'Entremont, A.; Pilon, L. *J. Power Sources* **2014**, *246*, 887–898.

(11) Janssen, M.; van Roij, R. *Phys. Rev. Lett.* **2017**, *118*, 096001.

(12) Gouy, M. *J. Phys. Theor. Appl.* **1910**, *9*, 457–468.

(13) Chapman, D. L. *Lond. Edinb. Dubl. Phil. Mag.* **1913**, *25*, 475–481.

(14) Stern, O. *Z. Elektrochem. Angew. P.* **1924**, *30*, 508–516.

(15) Schmickler, W., *Interfacial Electrochemistry*; Oxford University Press: 1996.

(16) Schmickler, W.; Henderson, D. *Prog. Surf. Sci.* **1986**, *22*, 323–419.

(17) Torrie, G. M.; Valleau, J. P. *J. Chem. Phys.* **1980**, *73*, 5807–5816.

(18) Boda, D.; Henderson, D.; Chan, K.-Y. *J. Chem. Phys.* **1999**, *110*, 5346–5350.

(19) Breitsprecher, K.; Košovan, P.; Holm, C. *J. Phys. Condens. Matter* **2014**, *26*, 284108.

(20) Härtel, A.; Janssen, M.; Samin, S.; van Roij, R. *J. Phys. Condens. Matter* **2015**, *27*, 194129.

(21) Zhou, S.; Lamperski, S.; Zydorczak, M. *J. Chem. Phys.* **2014**, *141*, 064701.

(22) Härtel, A.; Samin, S.; van Roij, R. *J. Phys.: Condens. Matter* **2016**, *28*, 244007.

(23) Overbeek, J. T. G. *Colloids Surf.* **1990**, *51*, 61–75.

(24) Marcus, R. A. *J. Chem. Phys.* **1955**, *23*, 1057–1068.

(25) Riemann, B., *Grundlagen für eine allgemeine Theorie der Functionen einer veränderlichten complexen Grösse*, 1851, pp 8–9.

(26) Biesheuvel, P.; Soestbergen, M. v. *J. Colloid Interface Sci.* **2007**, *316*, 490–499.

(27) Lue, L.; Zoeller, N.; Blankschtein, D. *Langmuir* **1999**, *15*, 3726–3730.

(28) Porada, S.; Weinstein, L.; Dash, R.; van der Wal, A.; Bryjak, M.; Gogotsi, Y.; Biesheuvel, P. *ACS Appl. Mater. Interfaces* **2012**, *4*, PMID: 22329838, 1194–1199.

(29) d'Entremont, A.; Pilon, L. *J. Power Sources* **2014**, *273*, 196–209.

(30) Kim, T.; Dykstra, J.; Porada, S.; van der Wal, A.; Yoon, J.; Biesheuvel, P. *J. Colloid Interface Sci.* **2015**, *446*, 317–326.

(31) Smith, D. W. *J. Chem. Ed.* **1977**, *54*, 540–542.

(32) Roussak, O. V.; Gesser, H., *Applied Chemistry, A Textbook for Engineers and Technologists*; Springer: 2012.

(33) Van Rijssel, J.; Erné, B. H.; Meeldijk, J. D.; Casavola, M.; Vanmaekelbergh, D.; Meijerink, A.; Philipse, A. P. *Phys. Chem. Chem. Phys.* **2011**, *13*, 12770–12774.

(34) Volkov, A.; Paula, S.; Deamer, D. *Bioelectrochemistry and Bioenergetics* **1997**, *42*, 13th International Symposium on Bioelectrochemistry and Bioenergetics, 153–160.

(35) Conway, B., *Ionic hydration in chemistry and biophysics*; Studies in physical and theoretical chemistry; Elsevier Scientific Pub. Co.: 1981.

(36) Varela, L. M.; García, M.; Mosquera, V. *Phys. Rep.* **2003**, *382*, 1–111.

(37) Gates, E. D., *Introduction to Electronics*; Cengage Learning: 2006.

(38) Rodenburg, H. P. Measurement and data treatment manual, Including software documentation, 2020.

(39) Soto, M. B.; Kubsch, G.; Scholz, F. *J. Electroanal. Chem.* **2002**, *528*, 18–26.

8 Appendix I: Derivation of the temperature difference equation

In general, a Wheatstone bridge looks like the circuit in Figure 39. There are four resistors which, in a balanced bridge, are of equal electrical resistance. The voltage across the bridge ΔV is zero when the bridge is balanced [37].

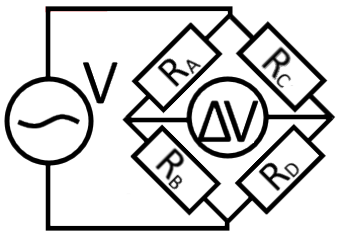

Figure 39: Wheatstone bridge circuit with an alternating current source.

If the bridge is not balanced, however, there is a non-zero voltage ΔV across the bridge. This voltage is equal to the difference in voltage over R_A and R_C.

$$\Delta V = V_A - V_C \tag{56}$$

The applied voltage is V, which means that $V_B = V - V_A$ and $V_D = V - V_C$. The voltages over R_A and R_C depend on the applied voltage and the values of both resistors in their respective branches of the parallel circuit.

$$V_A = V\left(1 - \frac{R_A}{R_A + R_B}\right) \tag{57}$$

$$V_C = V\left(1 - \frac{R_C}{R_C + R_D}\right) \tag{58}$$

Plugging Equations 57 and 58 into Equation 56:

$$\Delta V = V\left[\left(1 - \frac{R_A}{R_A + R_B}\right) - \left(1 - \frac{R_C}{R_C + R_D}\right)\right] = V\left[\frac{R_C}{R_C + R_D} - \frac{R_A}{R_A + R_B}\right] \tag{59}$$

If only one resistor differs from the others, as in the case with three reference thermometers R_e and a measuring thermometer R_M, the situation becomes simpler. In the present case, the measuring thermometer takes the place of R_D. Plugging $R_A = R_B = R_C = R_e$ and $R_D = R_M$ into Equation 59 gives:

$$\Delta V = V\left[\frac{R_e}{R_e + R_M} - \frac{1}{2}\right] \tag{60}$$

$$\frac{\Delta V}{V} = \frac{R_e}{R_e + R_M} - \frac{1}{2} \tag{61}$$

$$\frac{\Delta V}{V} + \frac{1}{2} = \frac{R_e}{R_e + R_M} \tag{62}$$

$$\frac{2\Delta V + V}{2V} = \frac{R_e}{R_e + R_M} \tag{63}$$

$$2VR_e = (2\Delta V + V)(R_e + R_M) \tag{64}$$

$$2VR_e = 2\Delta VR_e + VR_e + 2\Delta VR_M + VR_M \tag{65}$$

$$VR_e - VR_M = 2\Delta VR_e + 2\Delta VR_M \tag{66}$$

$$V(R_e - R_M) = 2\Delta V(R_e + R_M) \tag{67}$$

Introducing $R_e + R_M = R_e - R_M + 2R_M$:

$$V(R_e - R_M) = 2\Delta V(R_e - R_M + 2R_M) \tag{68}$$

Rearranging:

$$(V - 2\Delta V)(R_e - R_M) = 4\Delta VR_M \tag{69}$$

$$R_e - R_M = \frac{4\Delta VR_M}{V - 2\Delta V} \tag{70}$$

Defining $\Delta R = R_M - R_e$:

$$\Delta R = -\frac{4\Delta VR_M}{V - 2\Delta V} \tag{71}$$

The electrical resistance of a Pt100 RTD depends on temperature following $R = 100 + 0.385005T$. Consequently, the difference in resistance between the two resistors R_M and R_e is given by:

$$\Delta R = R_M - R_e = 0.385005(T_M - T_e) = 0.385005\Delta T \tag{72}$$

The quantity of interest is the temperature difference. Rearranging and combining Equation 72 with Equation 71 gives:

$$\Delta T = -\frac{1}{0.385005}\Delta R = -\frac{1}{0.385005}\frac{4\Delta VR_M}{V - 2\Delta V} \tag{73}$$

9 Appendix II: Software reference

All software used to record, analyse and plot data for this work has been written in Python 3, with the exception of the *ziControl* program for the *Zürich Instruments HF2LI*, the *VersaStudio* program for the *PARSTAT MC1000* and the *NOVA* program for the *Metrohm Autolab PGSTAT100*. Except for a small amount of Interactive Python code, all Python code is contained in scripts and can be easily accessed. The scripts are described in the *Measurement and data treatment manual* [38]. The required Python version and modules for running the scripts are listed in Table 4 and can also be found in the manual [38].

Name	**Version**	**Function**
Python 3	3.6 or higher	Core
NumPy	Most recent stable version	Mathematical operations
Matplotlib	Most recent stable version	Plotting
Argparse	Most recent stable version	Command line argument parsing
wxPython	Most recent stable version	GUI
PyVISA	Most recent stable version	SCPI (using NI-VISA)

Table 4: System requirements for using the Python scripts that have been designed for this work.

10 Appendix III: Validation of the calibration routine

To establish whether the scripts for calibration of the HFS and RTD setups, *CalibrateRTD.py* and *CalibrateHFS.py*, work correctly, test current data for which Π_{irr} and K can be calculated analytically can be generated. Such test current data comprise two rectangular peaks: a charging peak from t_0 to t_1 with height h_1 and a discharging peak from t_1 to t_2 with height h_2. The accompanying temperature data need not be generated: the charging and discharging temperature peak areas can simply be set to two constant values, B_1 and B_2. The calibration constant K then follows from Equation 74.

$$K = \frac{\int_{t_0}^{t_1} \psi_R(t) I(t)\,\mathrm{d}t + \int_{t_1}^{t_2} \psi_R(t) I(t)\,\mathrm{d}t}{B_1 + B_2} = \frac{\int_{t_0}^{t_1} \psi_R(t) h_1\,\mathrm{d}t + \int_{t_1}^{t_2} \psi_R(t) h_2\,\mathrm{d}t}{B_1 + B_2} \tag{74}$$

The potential over the solution, $\psi_R(t)$, takes the form of Equation 75. In this equation, Q_{full} is the total charge built up during charging.

$$\psi_R(t) = \psi\left[1 - \frac{Q(t)}{Q_{full}}\right] \tag{75}$$

In the case of rectangular peaks, an analytical expression exists for the integrals $\int_{t_0}^{t_1} \psi_R(t) I(t)\,\mathrm{d}t$ and $\int_{t_1}^{t_2} \psi_R(t) I(t)\,\mathrm{d}t$. Consider a current profile as in Figure 40. During charging, $Q(t)$ rises linearly to $Q_{full} = h_1 \times (t_1 - t_0) = h_1 \times t_1$. During discharging, it drops to $Q_{full} + h_2 \times t_2$.

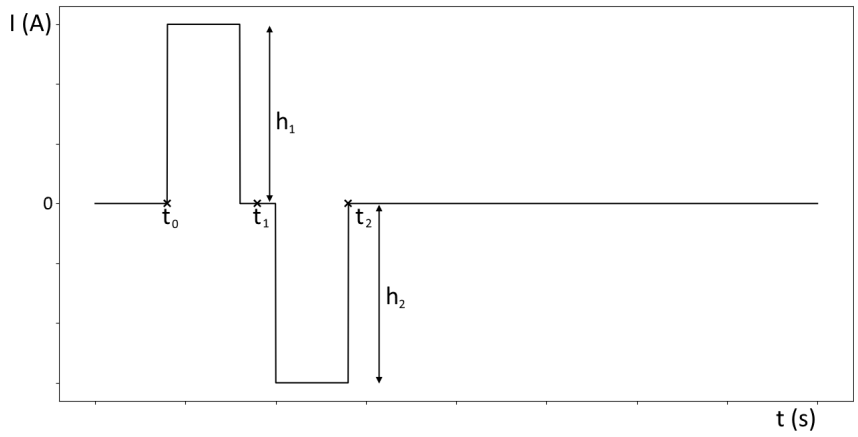

Figure 40: The general form of the model dataset with rectangular peaks.

In this specific situation, $\int_{t_0}^{t_1} \psi_R(t) I(t)\,\mathrm{d}t$ becomes:

$$\Pi_{irr}^{ch} = \int_{t_0}^{t_1} \psi_R(t) I(t)\,\mathrm{d}t = \int_{t_0}^{t_1} \psi\left[1 - \frac{Q(t)}{Q_{full}}\right] I(t)\,\mathrm{d}t = \psi h_1 \int_{t_0}^{t_1} \left[1 - \frac{h_1 \times t}{Q_{full}}\right] \mathrm{d}t \tag{76}$$

This works out to:

$$\psi h_1 \int_{t_0}^{t_1} \left[1 - \frac{h_1 \times t}{Q_{full}}\right] \mathrm{d}t = \psi h_1 \int_{t_0}^{t_1} \mathrm{d}t - \frac{\psi h_1^2}{Q_{full}} \int_{t_0}^{t_1} t\,\mathrm{d}t = \psi h_1 t_1 - \frac{\psi h_1^2 t_1^2}{2 Q_{full}} \tag{77}$$

Which can be further simplified:

$$\psi h_1 t - \frac{\psi h_1^2 t_1^2}{2 Q_{full}} = \psi h_1 t_1 \left[1 - \frac{h_1 t_1}{2 Q_{full}}\right] \tag{78}$$

Finally, the result takes the form of Equation 79.

$$\int_{t_0}^{t_1} \psi_R(t) I(t)\,\mathrm{d}t = \psi h_1 t_1 \left[1 - \frac{h_1 t_1}{2Q_{full}}\right] = \psi\left[Q_{full} - \frac{Q_{full}^2}{2Q_{full}}\right] \tag{79}$$

For the discharge, $\int_{t_1}^{t_2} \psi_R(t) I(t) dt$ does not take the same form, because $Q(t) = Q_{full} + h_2 \times (t_2 - t_1)$. For convenience, time is reset at the start of the discharge peak, such that $t_1 = 0$ and $Q(t) = Q_{full} + h_2 \times t_2$. Using this, Equation 80 is formulated.

$$\Pi_{irr}^{dis} = \int_{t_1}^{t_2} \psi_R(t) I(t)\,\mathrm{d}t = \int_{t_1}^{t_2} \psi\left[1 - \frac{Q(t)}{Q_{full}}\right] I(t)\,\mathrm{d}t = \psi h_2 \int_{t_0}^{t_1} \left[1 - \frac{Q_{full} + h_2 \times t}{Q_{full}}\right] \mathrm{d}t \tag{80}$$

This works out to:

$$\psi h_2 \int_{t_0}^{t_1} \left[1 - \frac{Q_{full} + h_2 \times t}{Q_{full}}\right] \mathrm{d}t = \psi h_2 \int_{t_0}^{t_1} \left[1 - \frac{Q_{full}}{Q_{full}} + \frac{h_2 \times t}{Q_{full}}\right] \mathrm{d}t = \frac{\psi h_2^2}{Q_{full}} \int_{t_1}^{t_2} t\,\mathrm{d}t \tag{81}$$

This can easily be integrated, which gives the final result for $\int_{t_1}^{t_2} \psi_R(t) I(t)\,\mathrm{d}t$:

$$\int_{t_1}^{t_2} \psi_R(t) I(t)\,\mathrm{d}t = \frac{\psi h_2^2}{Q_{full}} \int_{t_1}^{t_2} t\,\mathrm{d}t = \frac{\psi h_2^2 t_2^2}{2Q_{full}} \tag{82}$$

Using Equations 79 and 82, Equation 74 can be solved. The answer can then be compared to the numerical result obtained from the data treatment software. This has been done for various chosen values of ψ, B_1, B_2, h_1, h_2, $t_1 - t_0$ and $t_2 - t_1$. See Table 5.

ψ **(V)**	$\mathbf{h_1}$ **(A)**	$\mathbf{h_2}$ **(A)**	$\mathbf{t_1}$ **-** $\mathbf{t_0}$ **(s)**	$\mathbf{t_2}$ **-** $\mathbf{t_1}$ **(s)**	$\mathbf{B_1}$ **(Ks)**	$\mathbf{B_2}$ **(Ks)**
$\Pi_{irr}^{ch^a}$ **(J)**	$\Pi_{irr}^{dis^a}$ **(J)**	K^a **(J/(Ks))**	$\Pi_{irr}^{ch^n}$ **(J)**	$\Pi_{irr}^{dis^n}$ **(J)**	K^n **(J/(Ks))**	
0.5	3	−3	2	2	2.5	0.5
1.5	1.5	1	1.49325	1.50825	1.0005	
0.4	2	−2.5	2	1.5	2	0.75
0.8	0.703125	0.546591	0.796398	0.708167	0.547114	
0.2	−1	1.25	4	3.5	0.25	1.5
0.4	0.478516	0.502009	0.3992	0.470587	0.497021	

Table 5: Results of calibration using test data. Numerical results are given with as many decimals as the software would provide. Results marked with superscript a are analytical, whereas those marked with n are numerical.

The analytical and numerical results are found to be in good agreement. Any differences can easily be explained by the limited resolution of the test data, which always contains only 2000 data points. Therefore, it can be safely concluded that the data treatment software works correctly.

11 Appendix IV: Operation of the RTD setup

11.1 The calorimeter circuit

The circuit diagram of the calorimeter in the RTD setup is an unbalanced Wheatstone bridge with an alternating current source. See Figure 41.

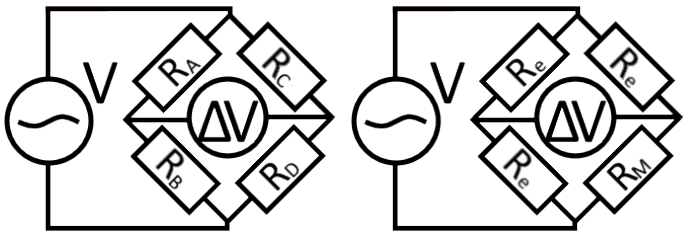

Figure 41: Wheatstone bridge circuit in its general form (LHS) and as it is implemented in the RTD setup (RHS).

The alternating current source is the second output channel of the *Zürich Instruments HF2LI* lock-in amplifier. Originally, it was the first output channel, but this channel ceased to function, presumably due to a voltage spike. The **IN** and **IN DIFF** inputs of channel 1 are used to determine the voltages across the two reference thermometers at the start of the opposite arms of the Wheatstone bridge, R_A and R_C. This allows the voltage ΔV across the Wheatstone bridge to be determined as $\Delta V = V(\textbf{IN})$ - $V(\textbf{IN DIFF})$. Lastly, half of the applied voltage is measured as the voltage across one of the reference thermometers using the **IN** input of channel 2.

11.2 Calculating the temperature difference

To calculate the temperature difference in the RTD setup, Equation 83 is used.

$$\Delta T = -\frac{1}{0.385005}\Delta R = -\frac{1}{0.385005}\frac{4\Delta V R_M}{V - 2\Delta V} \tag{83}$$

With the exception of R_M, all quantities in Equation 83 are measured. R_M is calculated via Equation 84, with $T = 22$ °C.

$$R = \frac{100 - T}{0.385005} \tag{84}$$

It may be best to change the setup to allow a direct measurement of the measuring thermometer's resistance R_M, but calculating it is not particularly objectionable.

11.3 Controlling the lock-in amplifier

The *Zürich Instruments HF2LI* is controlled via the *ziControl* program. The use of this program and two accompanying Python scripts is described in the *Measurement and data treatment manual* [38].

12 Appendix V: Problems and peculiarities

During the course of the project, several theoretical and practical problems have been encountered. Most of the important, unsolved problems are listed here.

12.1 Time stamps in the RTD setup

12.1.1 Lost seconds

Due to the data saving method used by the *Zürich Instruments HF2LI* lock-in amplifier, time stamps for $\Delta T(t)$ are not recorded live. While the instrument does indicate a sampling frequency, this is not the exact sampling frequency, and using it to determine the time is ill-advised.

Instead, the time of file creation t_c and the time of last modification t_m are used to determine the time stamps. The time between data points is assumed to be constant during the entire measurement, which means that, for a data point of index $i \in [0, 1, ..., N)$ in a dataset of N points, the time stamp is given by Equation 85.

$$t_i = \frac{i \times (t_m - t_c)}{N} \tag{85}$$

This is a reasonably accurate method, but it is not perfect. In all datasets, one second goes missing roughly every hour. This results in a tiny systematic error in the time.

12.1.2 Time zones and daylight savings

The Python script responsible for determining t_c and t_m is affected by the computer's internal clock and needs to be adjusted whenever the time zone changes from CET to CEST and from CEST to CET. Instructions can be found inside the script itself, *HF2Li_Reader.py* [38].

12.1.3 Time-outs

The *Metrohm Autolab PGSTAT100* potentiostat occasionally takes a longer time step between current data points. This happens when a different voltage is applied (ca. 10 s without new data) and when a large amount of data is saved (in excess of 60 s without new data). The former is generally not problematic, but the latter is. Saving is indicated in *NOVA* by double horizontal lines in the procedure. It is best to schedule saving at the end of charging or discharging. Note that this is only relevant in very long (>40 h) measurements, as saving is not necessary during shorter measurements.

12.2 The RTD setup's elevated baseline

As mentioned in section 3.2, unwanted resistances in the Wheatstone bridge circuit give rise to an elevated ΔT baseline, as these resistances lead to a non-zero ΔR, even when there is no temperature difference between the reference and measuring thermometers. The elevated baseline results from several phenomena.

The reference and measuring thermometers have different resistances in their leads, which is responsible for part of the elevated temperature difference baseline. This is mainly due to the Pt100s being used for two-wire sensing instead of the recommended three- or four-wire sensing. This leads to increased sensitivity, but also to differences in the thermometers' impedances. Note that these truly are impedances and not simple resistances, for they depend on the frequency.

There is also the issue of self-heating. The amplitude of the voltage applied to the Wheatstone bridge circuit is deliberately kept at a low $V_{LI} = 0.5$ V, as it is found that higher applied voltages lead to a further elevated baseline. This is due to self heating, which is stronger in the measuring thermometer than in the more massive reference thermometers.

12.3 Limited sizes of current datasets

Both potentiostats used in this work can only store a limited number of current data points. The *Metrohm Autolab PGSTAT100* will not save more than 10000 data points during charging or discharging, which makes measuring one point per second impossible when charging for three or more hours. For long charging and discharging periods, one point should be recorded every two or more seconds.

The *PARSTAT MC1000* averages current data points if measurements go on for too long. There are several HFS datasets in which the current data consists of points spaced by more than half a minute. No noteworthy attempts to address this have been made.

13 Appendix VI: Cyclic voltammetry combined with calorimetry

At one point, while recording cyclic voltammograms, it was realised that both setups' heat sensors could also be used to collect data during cyclic voltammetry. This would allow the heat data to be plotted against the potential data, as the time stamps would be known for both the calorimetric and electrical measurements. This turned out to be particularly effective with the HFS setup, for which an example measurement result is given in Figure 42.

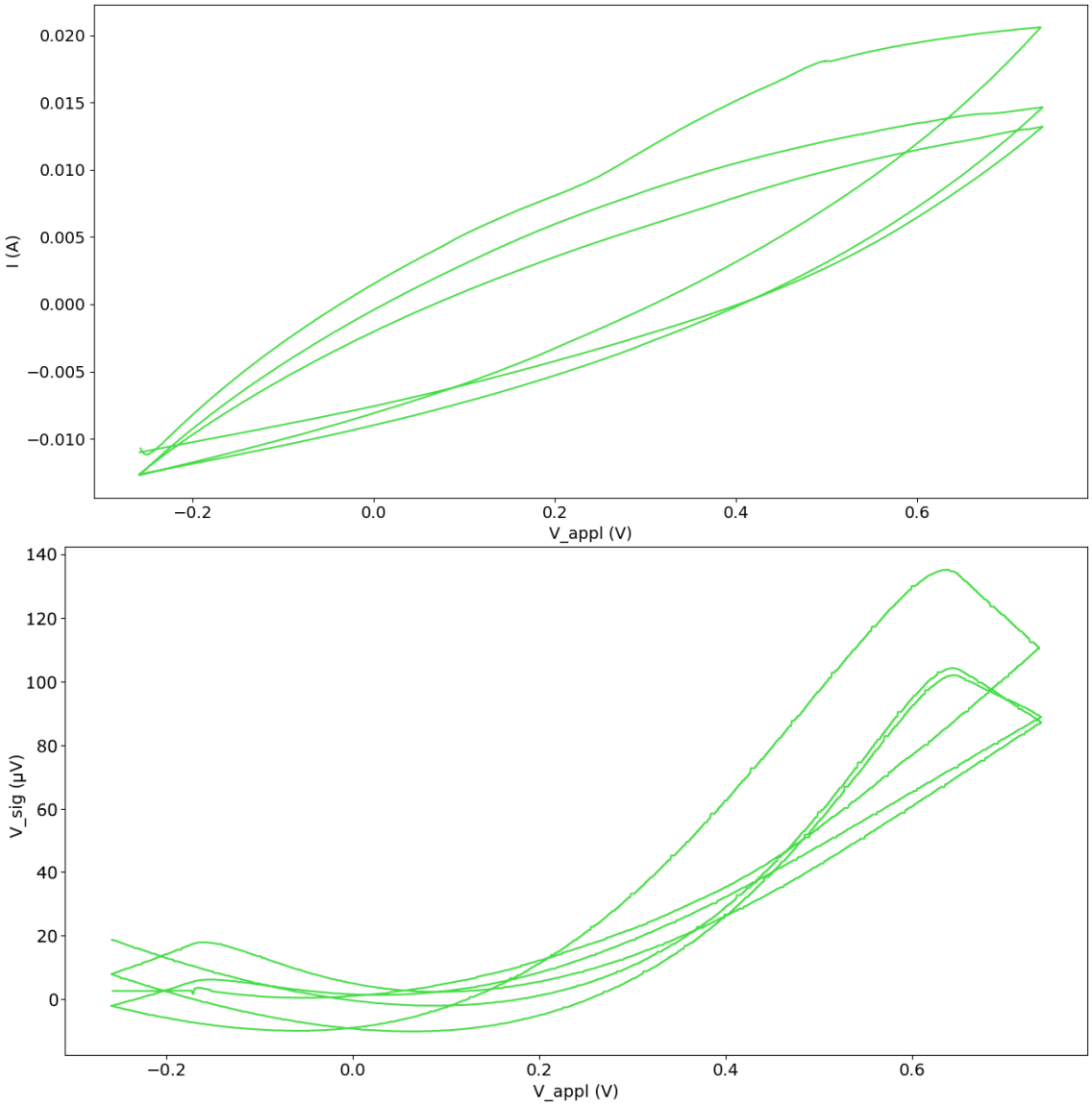

Figure 42: A cyclic voltammogram and its corresponding HFS signal. $\mathrm{d}V/\,\mathrm{d}t = 5\ \mathrm{mVs}^{-1}$. The applied potential is in V vs. Ag/AgCl/sat. KCl. Note that there is a slight difference between the start and end points of the two measurements.

Is should, however, be noted that this type of measurement is not new. Combined calorimetric and voltammetric measurements date back to 2002, when *Soto et al.* [39] used a thermistor inside an electrode to conduct measurements similar to the one in Figure 42. Interestingly, their

setup is much like our RTD setup. *Soto et al.* [39] also used a Wheatstone bridge for their measurements, although there is no mention of reference thermometers.